

DTIC FILE COPY

1

PSI-1032/TR-765

AD-A232 046

**MODELING OF THE LASER-INDUCED THERMAL RESPONSE, ABLATION, AND
FRAGMENTATION OF BIOLOGICAL TISSUE**

D. Rosen, G. Weyl, G. Simons, H. Petschek, and L. Popper
Physical Sciences Inc.
Research Park, P.O. Box 3100
Andover, MA 01810

ANNUAL REPORT

March 1987 to April 1988

**DTIC
ELECTE
MAR 14 1991
S D**

Contract No. N00014-87-C-0161

Distribution Statement

Office of Naval Research
Molecular Biology Division
800 N. Quincy Street
Arlington, VA 22217-5000

DISTRIBUTION STATEMENT A
Approved for public release
Distribution Unlimited

91 3 08 104

Unclassified

SECURITY CLASSIFICATION OF THIS PAGE

REPORT DOCUMENTATION PAGE

1. REPORT SECURITY CLASSIFICATION Unclassified			1b. RESTRICTIVE MARKINGS N/A		
2. SECURITY CLASSIFICATION AUTHORITY N/A			3. DISTRIBUTION / AVAILABILITY OF REPORT Distribution unlimited		
2b. DECLASSIFICATION / DOWNGRADING SCHEDULE N/A					
4. PERFORMING ORGANIZATION REPORT NUMBER(S) PSI 1032/TR-765			5. MONITORING ORGANIZATION REPORT NUMBER(S) N/A		
6. NAME OF PERFORMING ORGANIZATION Physical Sciences Inc.		6b. OFFICE SYMBOL (if applicable)		7a. NAME OF MONITORING ORGANIZATION DCASMA	
7. ADDRESS (City, State, and ZIP Code) Research Park. P.O. Box 3100 Andover, MA 01810		7b. ADDRESS (City, State, and ZIP Code) 495 Summer Street Boston, MA 02210-2184			
8. NAME OF FUNDING / SPONSORING ORGANIZATION Dept. of The Navy Office of Naval Research		8b. OFFICE SYMBOL (if applicable)		9. PROCUREMENT INSTRUMENT IDENTIFICATION NUMBER N00014-87-C-0161	
9. ADDRESS (City, State, and ZIP Code) 800 N. Quincy Street Arlington, VA 22217		10. SOURCE OF FUNDING NUMBERS			
		PROGRAM ELEMENT NO.		PROJECT NO.	TASK NO.
				WORK UNIT ACCESSION NO.	
11. TITLE (Include Security Classification) Modeling of the Laser-Induced Thermal Response, Ablation, and Fragmentation of Biological Tissue					
12. PERSONAL AUTHOR(S) D. Rosen, G. Weyl, G. Simons, H. Petschek, and L. Podder					
13a. TYPE OF REPORT Annual		13b. TIME COVERED FROM 3/87 TO 4/88		14. DATE OF REPORT (Year, Month, Day) 27 April 1988	
15. PAGE COUNT 15					
16. SUPPLEMENTARY NOTATION					
17. COSATI CODES			18. SUBJECT TERMS (Continue on reverse if necessary and identify by block number)		
FIELD	GROUP	SUB-GROUP	Free electron laser, medical applications, tissue ablation		
19. ABSTRACT (Continue on reverse if necessary and identify by block number)					
<p>This report describes the modeling activities carried out by Physical Sciences Inc. (PSI) during the first year of our ONR Contract N0014-87-C-0161. the objective of this contract is to develop models which can ultimately be used to predict the thermal response, ablation, and fragmentation of "hard" and "soft" biological tissue exposed to free electron laser (FEL) radiation. Most of our efforts thus far have been focused on the "hard" tissue problem, i.e., kidney stones, gallstones, calcified plaque.</p> <p>During this first year of the program modeling efforts have been initiated in four principal areas: (1) further development and application of 1-D and 2-D numerical heat conduction codes to model the thermal damage and ablation of soft tissue exposed to infrared laser energy, (2) modeling of plasma</p>					
20. DISTRIBUTION / AVAILABILITY OF ABSTRACT <input checked="" type="checkbox"/> UNCLASSIFIED/UNLIMITED <input type="checkbox"/> SAME AS RPT <input type="checkbox"/> DTIC USERS			21. ABSTRACT SECURITY CLASSIFICATION Unclassified		
22a. NAME OF RESPONSIBLE INDIVIDUAL Dr. Michael Marron			22b. TELEPHONE (Include Area Code) (202) 696-4513		22c. OFFICE SYMBOL Code 1141MB

→ initiation mechanisms in, and resulting plasma spectral emissions from, pulsed laser-irradiated kidney stones and gallstones, (3) modeling of laser-driven shock-induced fragmentation of kidney stones and gallstones, and (4) modeling of the above surface hydrodynamics, i.e., bubble growth and acoustic wave propagation, resulting from plasma-mediated laser energy deposition above a hard tissue surface in a fluid medium.

Whenever possible the predictions of the models are compared to available laser/tissue interaction data generated in the medical research community. Such model/data comparisons are vital for validating the models, guiding new model developments, and pointing out the need for additional critical experiments.

Accession For	
NTIS CRA&I	<input checked="" type="checkbox"/>
DTIC TAB	<input type="checkbox"/>
Unannounced	<input type="checkbox"/>
Justification	
By	
Distribution	
Availability Codes	
Dist	Avail. Code, or Special
A-1	



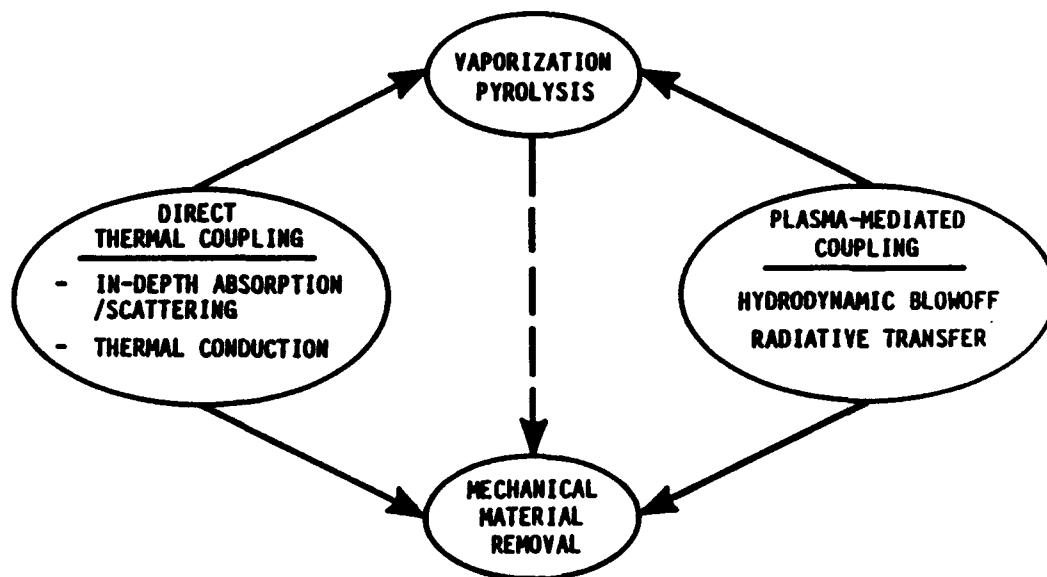
TABLE OF CONTENTS

<u>Section</u>		<u>Page</u>
1.	INTRODUCTION	1-1
2.	NUMERICAL MODELING OF THE LASER-INDUCED THERMAL RESPONSE AND ABLATION OF BIOLOGICAL TISSUE	2-1
2.1	Introduction	2-1
2.2	Description of Models Used	2-3
2.3	Model Predictions and Comparisons with Available Data	2-8
2.4	Summary and Conclusions	2-26
2.5	References	2-26
3.	PLASMA MODELING	3-1
4.	MECHANICAL FRAGMENTATION MODELING	4-1
5.	A SIMPLIFIED MODEL FOR LASER LITHOTRIPSY	5-1

1. INTRODUCTION

This report describes the modeling activities carried out by Physical Sciences Inc. (PSI) during the first year of our ONR Contract No. 0014-87-C-0161. The objective of this contract is to develop models which can ultimately be used to predict the thermal response, ablation, and fragmentation of "hard" and "soft" biological tissue exposed to free electron laser (FEL) radiation. Most of our efforts thus far have been focused on the "hard" tissue problem, i.e., kidney stones, gall stones, calcified plaque. A summary of the principal ablation mechanisms under consideration is presented in Figure 1-1.

The models developed are being used to identify the dominant physical processes and key parameters controlling the ablation/fragmentation process. Further, to validate the models, we are comparing their predictions, whenever possible, to available laser/tissue interaction data that have been generated in the medical research community. Model/data comparisons are vital for guiding new model developments. Similarly, the models help point out the need for additional critical experiments.



A-7910

Figure 1-1. Ablation mechanisms considered.

During this first year of the program, modeling efforts have been initiated in four principal areas: (1) further development and application of 1-D and 2-D numerical heat conduction codes to model the thermal damage and ablation of soft tissue exposed to infrared laser energy (Section 2); (2) modeling of plasma initiation mechanisms in, and resulting plasma spectral emissions from, pulsed laser-irradiated kidney stones and gallstones (Section 3); (3) modeling of laser-driven shock-induced fragmentation of kidney stones and gallstones (Section 4); and (4) modeling of the above-surface hydrodynamics, i.e., bubble growth and acoustic wave propagation resulting from plasma-mediated laser energy deposition above a hard tissue surface in a fluid medium.

Wherever possible, the predictions of the models have been compared to available data. The only exception is in the case of the mathematical models describing the above-surface fluid mechanics during laser lithotripsy. Numerical solutions to the relevant equations were not available in time to be incorporated into this report. Preliminary numerical results will, however, be presented at the upcoming contractors' review meeting.

2. NUMERICAL MODELING OF THE LASER-INDUCED THERMAL RESPONSE AND ABLATION OF BIOLOGICAL TISSUE

We present in this section detailed calculations of the thermal response and ablation of biological tissue exposed to 10μ laser radiation. For most of the calculations shown, tissue response was modeled using generalized computer codes that were originally developed to model the laser-induced response of a variety of non-biological materials. The models are applicable at any wavelength for which the absorption cross section in the tissue is large compared to the scattering cross section.

In this initial study, we have modeled soft tissue as a single component material with thermal and optical properties very similar to that of water. The predominant phenomena treated are in-depth laser absorption, thermal conduction, and surface vaporization. In-depth thermal damage of tissue is calculated by incorporating into the codes a reaction for the thermal denaturation of tissue protein.

Model calculations are presented for exposures ranging from low power CW exposures of a few watts per cm^2 and exposure times of tens of seconds to single-pulse exposures with peak irradiances of several megawatts per cm^2 and microsecond exposure durations. Where possible, model predictions are compared to available experimental data and the implications of the comparisons are discussed. Recommendations for future modeling improvements are also presented.

2.1 Introduction

In recent years, there have been a significant number of research studies directed at understanding the response of biological tissue to laser irradiation.¹ A major area of interest has been the laser-induced thermal response and ablation of tissue for surgical treatments,²⁻⁵ with perhaps the most prominent applications being tissue cutting and tissue welding procedures. The motivation has been to help define the laser treatment control

parameters for best achieving the desired beneficial effects of the laser, i.e., controlled heating, coagulation, cutting and hemostasis, and minimizing the undesired effects, i.e., unwanted damage to adjacent healthy tissue.

We report here the results of efforts we have initiated to develop detailed models of laser interactions with biological tissue. The overall objective has been to establish a well-founded theoretical understanding and validated predictive capability for characterizing a wide variety of medical treatments involving laser/tissue interactions. The ultimate aim is to develop predictive models that are both reliable and versatile and which can be used for optimizing the design of medical lasers as well as the surgical/clinical techniques by which they are applied.

The specific approach has been to apply detailed heat conduction and ablation codes originally developed for use with non-biological materials⁶ to the problem of biological tissue interactions. For the present studies, the scope has been focused on modeling primary tissue response to 10 μ m laser irradiation. However, the models developed can be applied at any laser wavelength for which absorption dominates over scattering and the absorption depth in tissue is known. For example, work is now underway at modeling tissue interactions at the Erbium:YAG laser wavelength ($\lambda \approx 3 \mu\text{m}$).

Interactions for a wide range of laser temporal waveforms and intensities have been studied. The models have been applied to single-pulse, repetitively-pulsed, and continuous wave (CW) irradiations. We present here only the results for CW and single-pulse exposures. Exposure times have been investigated from the single-pulse microsecond regime to CW exposures of tens of seconds. Irradiances have been varied from as low as 2 W/cm² to peak irradiances as high as 3 MW/cm². Although most of the calculations have been performed in the limit of one-dimensional heat conduction, predictions are also presented in which two-dimensional heat conduction effects have been modeled in detail. The latter were obtained using a three-dimensional heat conduction and ablation model.

Tissue material properties have been modeled rather simply. Tissue has been treated as a single-component homogeneous material with thermal proper-

ties quite similar to those of water. This assumption is very reasonable for high water content tissue such as fresh dermal or mucosal tissue.

Where possible, model predictions have been compared to available experimental data. The most detailed comparisons have been made with the experiments of Takata et al.⁷ and Walsh et al.⁸ The former studies investigated the thermal damage of pig skin induced by CW CO₂ laser radiation at low power irradiations of $1 < I < 9 \text{ W/cm}^2$. In the latter investigations, tissue ablation was studied using a pulsed TEA CO₂ laser.

2.2 Description of Models Used

With the exception of a simple analytical laser blow-off model (presented in a following subsection), all the modeling performed in this study was carried out using numerical heat conduction and ablation codes⁶ developed previously at Physical Sciences Inc. (PSI). These codes have been exercised extensively over many years to analyze the response of a wide range of non-biological materials exposed to a variety of high power lasers. Two different codes have been used: 1) a generalized ablation code that treats heat conduction in only one dimension, but which incorporates the ability to model in detail a wide range of ablation phenomena; and 2) a three-dimensional ablation code that can model radial as well as axial heat losses, but is more limited in its treatment of material ablation. In general, the single-pulse calculations have been performed using only the one-dimensional ablation code. For the single-pulse calculations, a one-dimensional analysis is clearly appropriate as radial heat conduction can be shown to be negligible over the time scale of an individual pulse.

A brief description of the numerical codes is presented below.

2.2.1 One-Dimensional Laser Effects Code

This code is a transient, thermal conduction model that can be used to treat a system comprised of up to three components. For organic composite materials, for example, it treats fiber (or a non-decomposing homogeneous component), resin and char. The latter two are associated with the organic

(pyrolyzing) components of the system, but have not been employed to date for medical applications since we have used a simple, single-component description of tissue for our initial studies. The one-dimensional code is complemented by a variety of subroutines dealing with specific laser-induced phenomena that one may wish to model according to the application.

The external laser heating can be CW, single pulse, or repetitively pulsed. Energy transfer mechanisms that can be treated in the code are:

- o Surface and/or internal absorption of laser energy
- o Surface vaporization
- o Internal pyrolysis
- o Surface thermal radiation
- o Energy transported by heated gaseous pyrolysis products, and
- o Convective heating (cooling) at the surface in external cross flow.

The conservation and transport of energy is governed by the following equation

$$\rho c \frac{\partial T}{\partial t} = \frac{\partial}{\partial x} \left(K \frac{\partial T}{\partial x} \right) - \dot{\rho}_r Q_p - \dot{\rho}_f H_v + \dot{m}_g c_g \frac{\partial T}{\partial x} - \frac{dI}{dx} \quad (1)$$

where ρ is the density, c is the specific heat, t is the time coordinate, x is the space coordinate; K is the thermal conductivity, $\dot{\rho}_r$ is the time rate of change of "resin" density, $\dot{\rho}_f$ is the time rate of change of "fiber" density, Q_p is the heat of pyrolysis of the resin, H_v is the heat of vaporization of stable products, \dot{m}_g is the mass flux of gaseous pyrolysis products, c_g is the specific heat of gaseous pyrolysis products, and I is the laser irradiance. In applying this code to tissue, the most straightforward approach has been to treat the water as a "fiber" component and any non-aqueous components as "resin". As mentioned earlier, the term "fiber" is used here to represent any homogeneous component of the material which is non-decomposing (but can undergo a phase change). For the present studies, however, tissue has been treated as if consisting of 100 percent "fiber" having the thermophysical properties of water. In future work, a multicomponent treatment is planned in which the non-aqueous constituents will also be modeled and treated as a "resin" component that can undergo pyrolysis and charring.

The inputs required by this model are: the target geometry; the target boundary and initial conditions; vaporization and pyrolysis rate equations (if pyrolysis is modeled); temperature-dependent thermophysical properties; reflectance; laser penetration depth in the material as a function of space and temperature; and the intensity and spatial profile of the laser irradiation. The effect of laser wavelength is treated by an appropriate choice of tissue reflectance and laser penetration depth.

The energy equation is solved with two (front and back) boundary conditions and one initial condition using an explicit, forward-marching, finite-difference technique. The (moving) coordinate system is located on the receding front surface and the numerical scheme is optimized by means of a grid which expands in time and sheds grid points as the material decreases in thickness.

The outputs that can be provided by the model are: the transient mass removal and pyrolysis rates; the transient "resin" and char density; the transient temperature distribution; and an energy balance of the target material, i.e., thermal energy residing in the target and energy lost to vaporization, reradiation, etc.

2.2.2 Three-Dimensional Model

The three-dimensional model accounts for transient heat conduction in two- (radial symmetry) or three-dimensional cartesian or cylindrical polar coordinates. This model can treat a variety of features, including anisotropic materials, temperature-dependent thermophysical properties, in-depth energy absorption, reflection, and surface radiative and convective heat transfer at the boundaries of the material. At the present time, surface ablation is simulated in the three-dimensional code by means of a melting process (i.e., fixed vaporization/melt temperature). This is in contrast to the one-dimensional model where the vaporization rate, not the vaporization temperature, is an input.

The three-dimensional code uses an implicit numerical technique which can range from the standard Crank-Nicholson formulation to the classical succes-

sive overrelaxation implicit procedure. The inputs required by this model are essentially the same as those required by the one-dimensional model described earlier. The outputs of this model are ablation contours at various times and the transient-temperature distributions in the target material.

2.2.3 Code Modifications for Present Studies

In general, the codes were used with minimal modifications with only the input changed to reflect the thermophysical properties of biological tissue (see discussion that follows on tissue material properties). The only new physical mechanism added that was not previously in the codes is the reaction that gives rise to the thermal damage or necrosis of tissue, i.e., denaturation of tissue protein. Following the work of Henriques⁹ and others,¹⁰⁻¹² an equation for damage was employed for a cylindrical coordinate system of the form:

$$\Omega(r,z) = A \int_{t_i}^{t_f} \exp\{-E_a/RT\} dt \quad (2)$$

where

- r, z = cylindrical coordinates
- A = preexponential factor (s^{-1})
- E_a = activation energy for the reaction (J/mole)
- R = universal gas constant = 8.3 J/mole K
- T = $T(r, z, t)$ = tissue temperature (K)
- $\Omega(r, z)$ = damage integral
- t_i = onset time of laser exposure
- t_f = time after laser exposure when tissue recovers to its ambient temperature

The above damage equation is expressed in the familiar Arrhenius form used throughout the literature on thermally-induced tissue damage. The specific values for A and E_a used in the calculation and the basis for their selection are presented in the following subsection.

2.2.4 Tissue Material Properties

For this initial modeling effort, biological tissue has been modeled as a single component material with constant thermal and optical properties similar to those of water. The philosophy was to begin our analysis with a nominal baseline set of material properties and then to vary the laser irradiation conditions to explore the sensitivity of the results to laser parameters. In general, the properties we have used should be representative of high water content tissue, i.e., mucosa,¹³ dermal layers,² etc. The validity of our thermal properties has been tested, at least in part, by comparing our model predictions with a fairly extensive body of data on laser-induced thermal damage in pig skin.⁷ The results of those comparisons are presented in the following section. Table 2.1 presents the values of the tissue materials properties used in our calculations.

TABLE 2.1. Tissue Thermophysical Properties Used for Model Calculations.

Thermal/Optical Properties

Density, $\rho = 1.05 \text{ g/cc}$

Specific Heat, $C = 4 \text{ J/g-K}$

Thermal Conductivity, $k = 6.8 \times 10^{-3} \text{ Wcm-K}$;

Thermal Diffusivity, $\kappa = k/\rho C = 1.6 \times 10^{-3} \text{ cm}^2/\text{s}$

Heat of Vaporization, $H_v = 2257 \text{ J/g}$

Absorption Coefficient ($\lambda = 10.6\mu$) = 769 cm^{-1} ($a = 13\mu$)

Emissivity (for thermal reradiation) = 1

Coefficients in Denaturation Equation (See Eq. (2))

$A = 3.1 \times 10^{98} \text{ s}^{-1}$

$E_a = 150,000 \text{ cal/mole} = 628,000 \text{ J/mole}$

From Ref. 9

Future improvements in the treatment of tissue material properties should incorporate material properties that are a function of the laser-modified water content.^{2,7} It is also desirable to provide a realistic treatment of the pyrolysis and possible charring of the organic, non-aqueous constituents of the tissue.

2.2.5 Temperature-Dependent Vaporization Rate

For the present work, one improvement we have made over previous analyses is the incorporation of a tissue vaporization rate that is a function of temperature. This has been accomplished by use of a mathematical fit to the equilibrium vapor pressure of water for various temperatures¹⁴ and coupling the resulting expression to a detailed treatment of the Knudsen layer* fluid dynamics of a surface vaporizing into a one atmosphere background.¹⁵ Thus, the surface vaporization temperature reached during a laser exposure is actually a function of the absorbed laser flux, with higher laser fluxes supporting higher mass vaporization rates, and consequently, higher surface temperatures. This improvement yields more realistic tissue temperature profiles (surface temperatures which can exceed 100°C) and, as a result, should give more accurate predictions of the resulting subsurface tissue damage.

2.3 Model Predictions and Comparisons with Available Data

2.3.1 Low Power CW Exposures

As an initial evaluation of the basic thermal response model, we first tested it against available tissue response data taken under low power conditions. Under these conditions, which are below the threshold for significant

* The Knudsen layer is a narrow region just above the vaporizing surface (a few mean free paths) in which the gas particles undergo sufficient collisions to achieve translational equilibrium and for the gas phase distribution function to be described by a full Maxwellian.

tissue vaporization, the absorbed laser flux goes into residual thermal energy of the tissue. The resulting thermal damage is a function of the tissue thermal properties only (density, specific heat, thermal conductivity), and the rate constant for the thermal denaturation reaction.

An excellent set of data exists from a series of investigations carried out on laser-induced thermal damage of skin.⁷ In those studies, Takata and coworkers irradiated pig skin with CO₂ and ruby lasers and made histologic determinations of the extent of thermal damage. The CO₂ experiments were performed with average CW powers between 1.5 and 2W, Gaussian beam profiles, and exposure durations from a few tenths of a second to several tens of seconds. Two different beam spot sizes were employed with $1/e^2$ radii of 0.71 and 0.383 cm, respectively, resulting in peak on axis irradiances of $1 < I_0 < 9 \text{ W/cm}^2$.

In Figures 2.1 and 2.2, we show typical comparisons of the predicted maximum depths of irreversible damage ($\alpha \approx 0.5 \rightarrow 1$)¹² with the corresponding observations.⁷ Our predictions are the dashed curves, the observations are

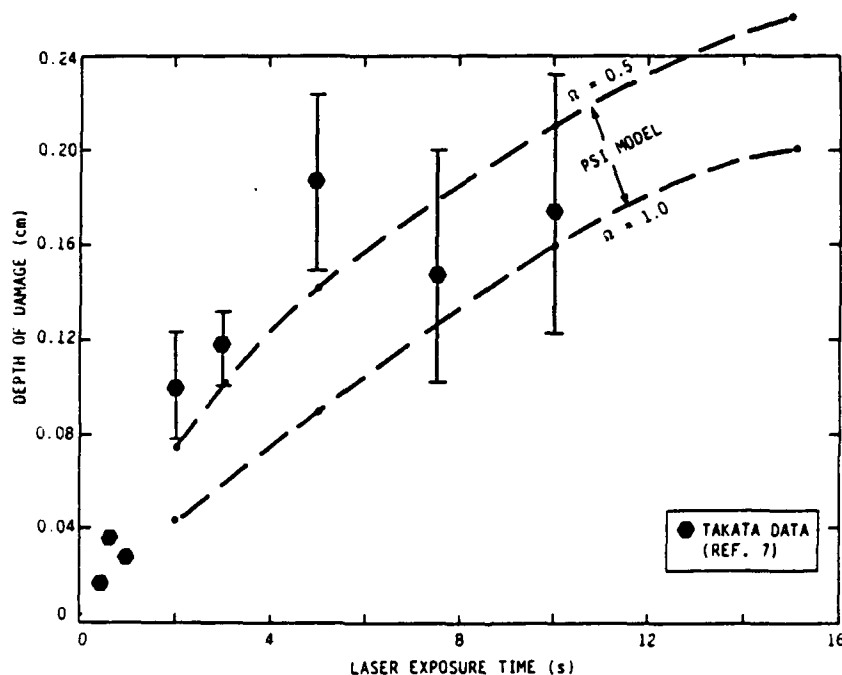
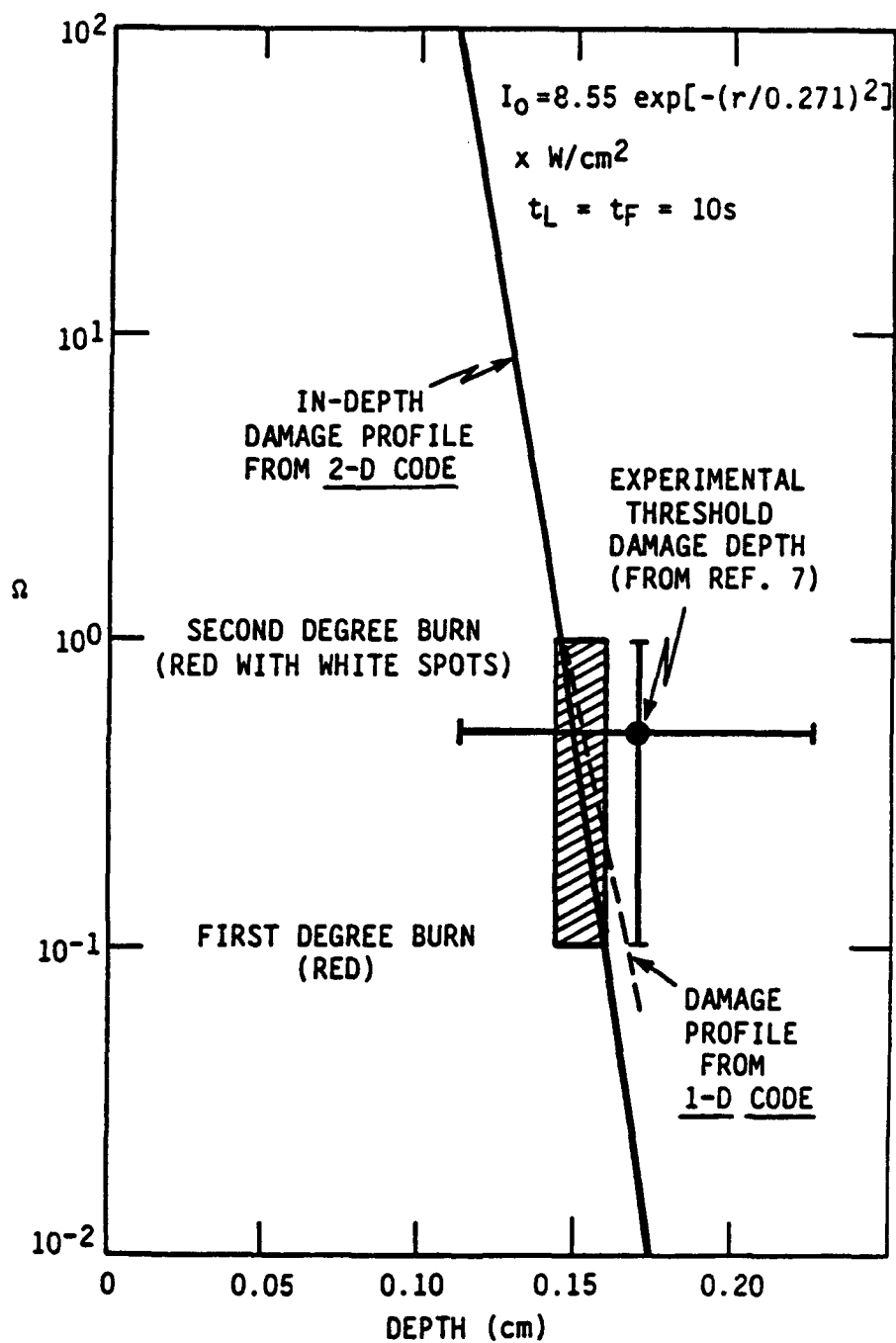


Figure 2-1. Model/data comparisons of depths of irreversible tissue damage produced by CO₂ laser exposures, $I_0 = 8.55 \text{ W/cm}^2$.



A-3042

Figure 2-2. Model/data comparison in in-depth tissue damage by CO₂ laser (one-dimensional versus two-dimensional code predictions and experimental data).

the reported data points with error bars, and the solid curves are the predictions of a model developed by Takata et al.⁷ As can be seen, the agreement between our model predictions and the measurements is generally quite good, especially considering the rather large error bars associated with the data.

For the calculations shown, the one-dimensional heat conduction code was used with the irradiance input being the peak on-axis value corresponding to each experiment and the laser exposure duration also the same as the experiment. Thus, the one-dimensional calculation was used to predict the depth of thermal damage occurring on axis (at the center of the spot). Of course, the measured maximum depths of damage also correspond to on-axis values. Two-dimensional calculations run subsequently indicated similar depths of axial thermal damage clearly showing that, at least for the range of conditions modeled, lateral heat conduction losses were not a major factor. Figure 2.2 shows a comparison between the predictions of the one- and two-dimensional heat conduction codes.

It should be noted that for most of the laser exposure conditions modeled, a significant amount of thermal damage continues to occur even after the laser is shut off. This is clearly a result of the heat conduction or "thermal soak" that takes place subsequent to the laser exposure. In general, it was found that to assess the final extent of thermal damage accurately, it was necessary to follow the thermal relaxation profile for at least one full exposure duration after termination of laser irradiation.

The one-dimensional calculations can predict fairly accurately the depths of damage observed in the Takata experiments on axis. However, it is clear that for predicting radial profiles of thermal damage, particularly when Gaussian beams are used, a two-dimensional code is desirable. The results of such calculations are shown in Figure 2.3. As can be seen, with a threshold damage criterion of $0.1 < Q_t < 1$, the predicted and observed damage radii are in close agreement.

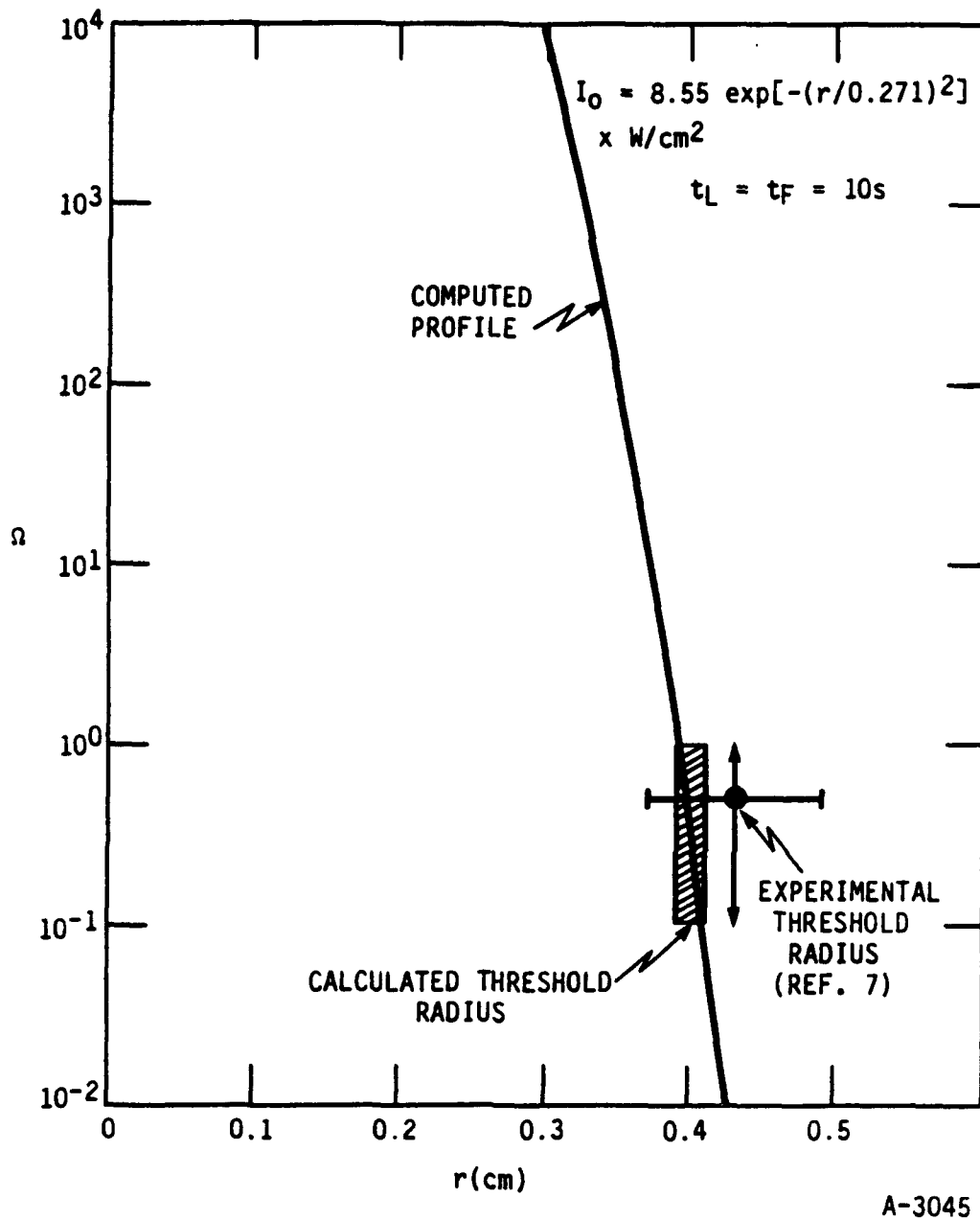


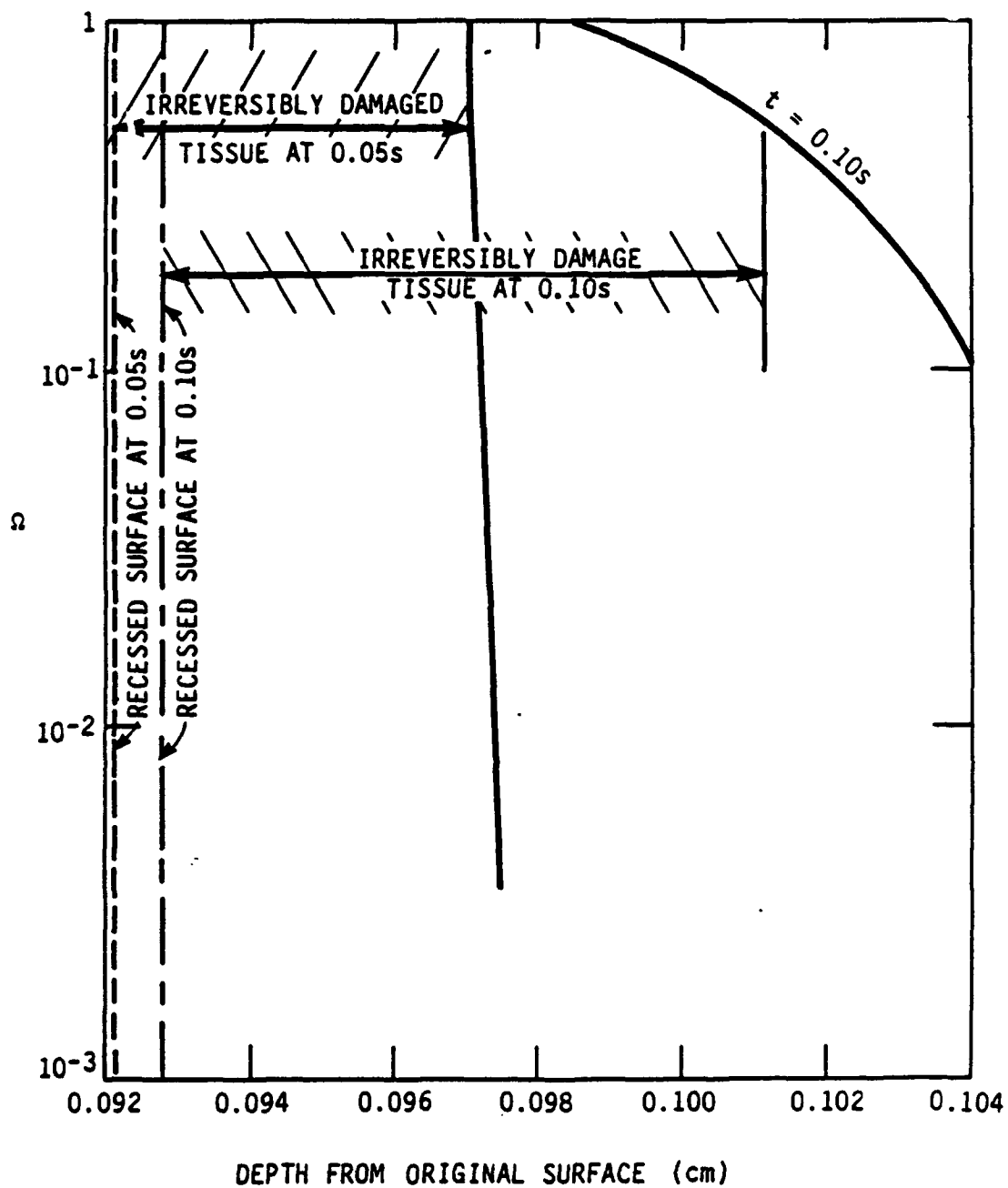
Figure 2-3. Calculated radial profile of damage at tissue surface versus experimentally measured radius of "threshold" damage.

2.3.2 Mid to High Power CW Exposures

Calculations have been performed for CW irradiations ranging from 250 W/cm² to 5 KW/cm² and with exposure durations as short as 10⁻²s and as long as 10s. Outputs of the code included mass loss, surface recession (i.e., crater depth), residual thermal energy, spatial/temporal temperature profiles, and profiles of the damage integral (Q). At least for the higher irradiances considered, we have found that steady state conditions are predicted to occur early in the laser exposure (within approximately 3 ms), at which time the surface temperature, recession rate, and residual thermal energy all assume constant values until the laser shuts off.

The computed in-depth temperature profiles and damage integral (Q) contours are plotted in Figures 2.4 and 2.5 for an incident irradiance of 5 kW/cm² before the laser shuts off and 0.05s later. (Note that the depths are given in reference to the original tissue surface and that there has been approximately 0.9 mm of tissue recession.) An interesting feature of Figure 2.5 is that, while the laser is on, the peak temperature is predicted to occur beneath the surface. Other researchers modeling laser-induced vaporization of solid materials with in-depth absorption have predicted similar temperature profiles.¹⁶ For example, in Ref. 16 it was found that "for certain laser and material parameters, subsurface temperatures will significantly exceed the surface temperature, and, under such conditions, explosive removal of material could occur, resulting in very rapid and efficient material removal."

It is interesting to note (from Figure 2.4) that while there is <1 percent additional contribution to tissue recession after the laser shuts off, the zone of in-depth thermal damage grows by about 60 percent (from ~50 μ m to ~80 μ m). This demonstrates that modeling the in-depth conduction of residual heat after the laser shuts off is important for accurately predicting the extent of thermal damage. This will become even more critical when dealing with short pulse interactions.



A-3053

Figure 2-4. Computed in-depth damage profiles after CW irradiation of 5 kW/cm^2 (laser exposure time is 0.05s).

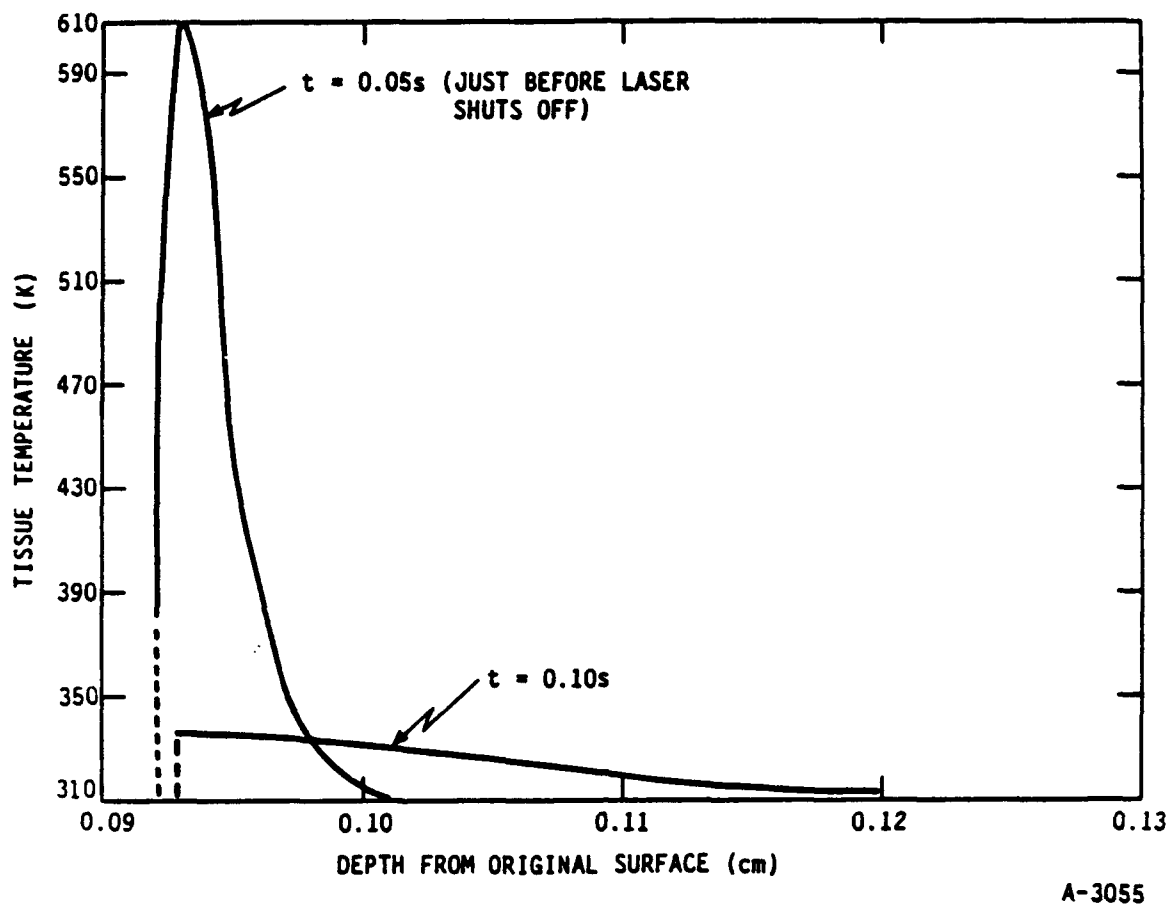


Figure 2-5. Computed in-depth temperature profiles in tissue ($I_0 = 5 \text{ kW/cm}^2$, exposure duration = 0.05s).

In Table 2.2 we summarize the results of four CW calculations run for irradiances of 250, 1300, 2000, and 5000 W/cm^2 with exposure times of 1, 0.19, 0.125, and 0.05s, respectively. The objective was to generate the same exposure fluence (250 J/cm^2) at several different irradiance levels and to compare their relative effect on recession and the extent of residual thermal damage. One of the more interesting quantities in Table 2.2 is $Z_r/\Delta Z_d$ or the ratio of the recession depth to the residual depth of irreversible tissue damage. Clearly, if the goal is to optimize tissue cutting while minimizing the extent of residual tissue damage, then larger values of $Z_r/\Delta Z_d$ are desirable. It is clear from Table 2.2 that the smallest relative amount of residual damage is achieved when operating at the highest irradiance level and shortest exposure time. These results provide quantitative support for a prevailing opinion that has now become increasingly evident in the laser treatment literature.¹⁷⁻¹⁹

TABLE 2.2. Comparison of CW Laser Exposures at Different Irradiance Levels But Fixed Exposure Fluence (250 J/cm²).

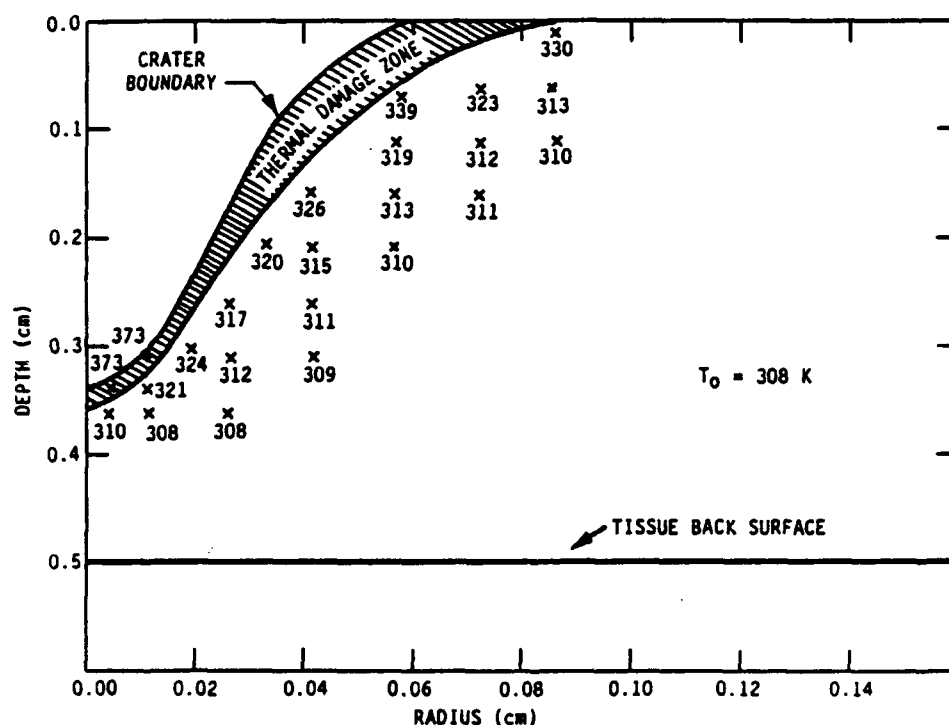
Irradiance (W/cm ²)	Exposure Duration (s)	Q_r^+ (J/cm ²)	Z_r^+ (cm)	ΔZ_d^+ (cm)	$Z_r/\Delta Z_d$
250	1.00	4.83	0.1048	0.0244	4.3
1300	0.192	2.77	0.1144	0.0144	7.9
2000	0.125	2.44	0.1133	0.0125	9.1
5000	0.050	1.91	0.0928	0.009	10.3
^+Q_r = final tissue residual energy ^+Z_r = final tissue recession depth $^+\Delta Z_d$ = final <u>residual</u> depth of irreversible tissue damage					

It is worth mentioning, however, that there are generally other factors which set upper limits to the irradiance level (and, correspondingly, lower limits to the pulse duration) which is most useful for clean, efficient, well-controlled ablation. One of these factors is the laser penetration depth. For example, it is expected that little value will be gained by decreasing the exposure duration to much less than δ^2/K where δ is the optical penetration depth and K is the thermal diffusivity of the material. Beyond this point, the deposition of heat during the laser exposure time will be controlled more by the scale length of the optical deposition than by thermal conduction. Other factors which may come into play at high irradiance levels are explosive material blow-off phenomena and the effects of plasma formation. Depending on the situation, such processes could be undesirable.

It should also be mentioned that the assertion that operating at higher irradiances and shorter exposure times produces less residual damage is necessarily true only if the spot size is kept constant. If, on the other hand, the higher irradiance is achieved by focussing to a smaller diameter spot, radial heat conduction losses and the relative extent of lateral thermal damage may increase.

Figure 2.6 demonstrates the ability of the two-dimensional code to predict the growth of residual thermal damage around the perimeter of a small spot crater. A two-dimensional calculation was run for a Gaussian beam with an intensity profile of $I(r) = 1990 \exp[-(r/0.031)^2]$ W/cm² (1/e radius = 310 μ m) and exposure duration of 0.5s. Figure 2.6 presents the computed results for the crater profile, the zone of residual thermal damage, and temperatures at selected points in-depth in the tissue.

It would be extremely valuable to test model predictions of the type shown in Figure 2.6 against comparable experimental data. Unfortunately, we have not yet found an appropriate body of data taken at these higher fluxes



A-3054

Figure 2-6. Calculated two-dimensional crater profile and temperature map at 0.5s ($P_0 = 6W$, $I = 1990 \exp[1-(r/0.031)^2]$).

which is of acceptable quality. In particular, most of the tissue cutting data available in the literature lacks an adequate specification of the laser beam spatial intensity profile that was used. A major goal of future efforts should be to acquire well-characterized and well-diagnosed laser/tissue ablation data to serve as a rigorous test of the models that have been developed and to determine where improvements are needed.

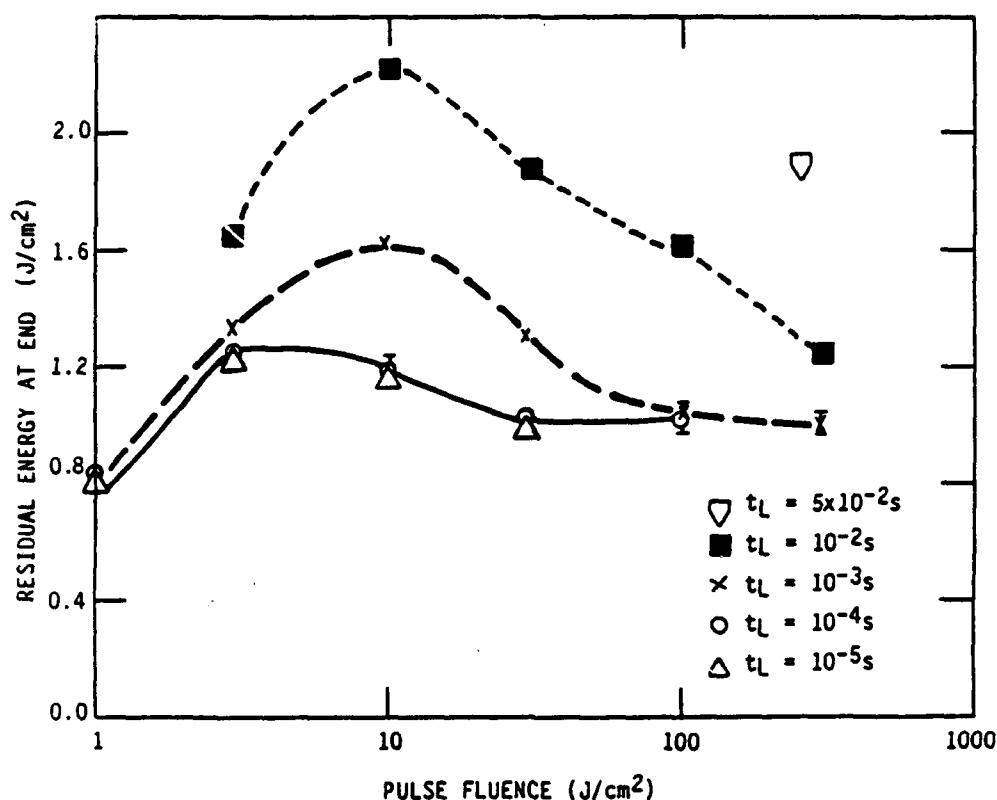
2.3.3 Modeling of Short, Single-Pulse Exposures

It is possible with present surgical CO₂ lasers to deliver laser energy to a treatment site in a variety of enhanced pulsing modes. In these modes, the laser is electronically pulsed to generate higher peak powers (up to a factor of 5 to 7 above the average CW power) in short repetitive bursts (presently 10⁻⁴ to 10⁻³s in duration). A considerable body of data in the laser surgical literature indicates that this enhanced or "super-pulsed" mode of operation can yield cleaner cuts with less residual damage to adjacent tissue. It should be mentioned, however, that these assertions are not without controversy. In addition, there is now a developing data base for which pulsed operation is being extended down to the microsecond (10⁻⁶s) regime.^{8,19} Based on preliminary analyses of the latter experiments, even more interest is being generated in the potential of using short pulses for achieving "clean" tissue cutting.

Code Predictions

To address some of these issues, the one-dimensional ablation code was used to run a series of single-pulse calculations for a range of pulse fluences varying from 1 to 100 J/cm² per pulse and for pulse durations from 10⁻⁵ to 10⁻²s. Typical results are presented in Figures 2.7 and 2.8.

Figure 2.7 is a plot of the calculated residual thermal energy in the tissue just after the ablation stops. The ratio of this quantity to the incident pulse fluence is the thermal coupling coefficient. Note that at the higher pulse fluences, i.e., ≈ 100 J/cm², the thermal coupling coefficient is predicted to be small, ~ 1 to 2 percent. The reason is that the energy deposition rate is so high that steady state vaporization of the tissue is



A-3052

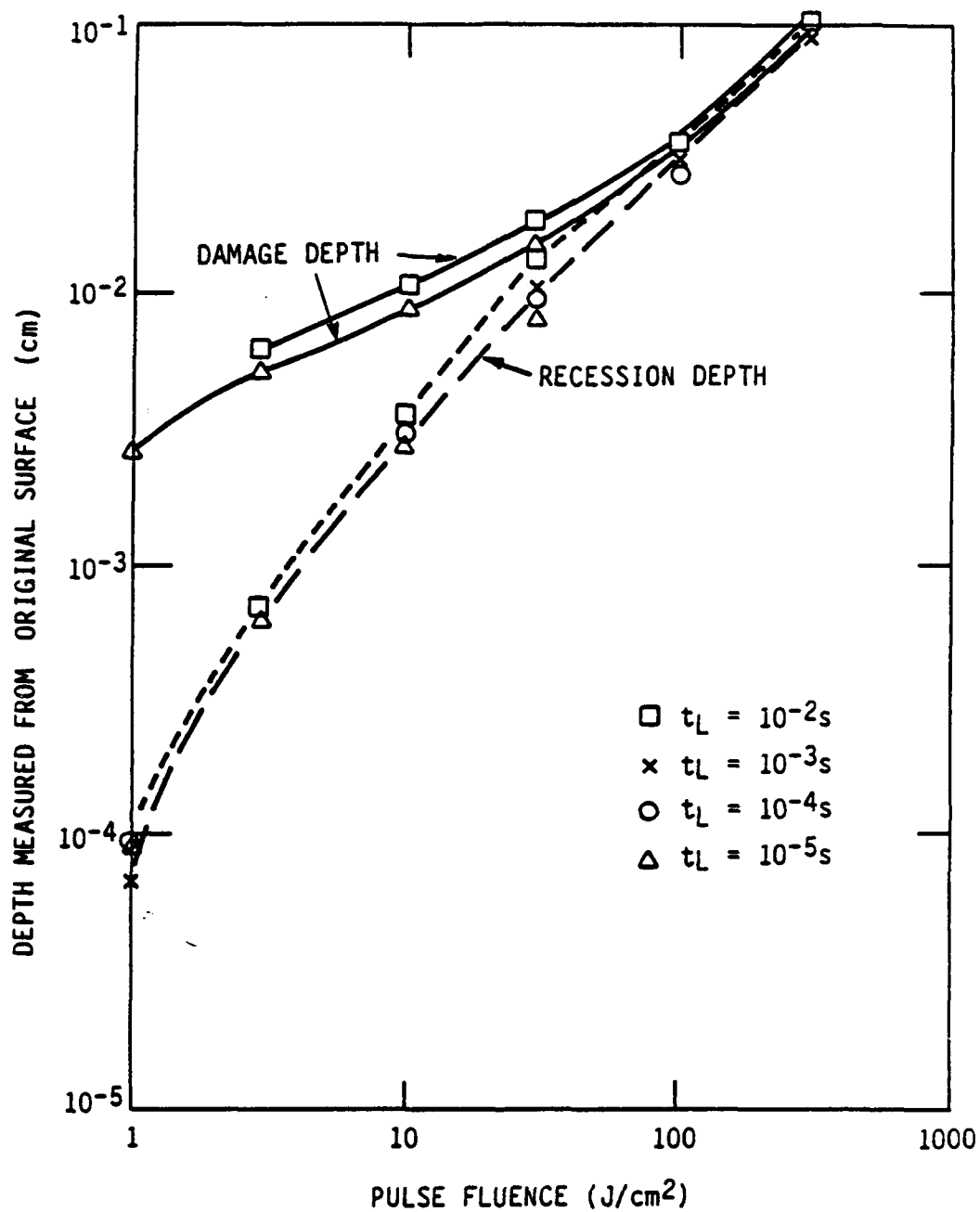
Figure 2-7. Calculated residual thermal energy in tissue as a function of pulse fluence for several different pulse durations.

achieved early in the pulse, so that the remainder of the pulse energy is simply carried off by vaporization products.

In Figure 2.8 we present the corresponding calculations of the recession depth and depth of thermal damage (relative to the original surface location). The depth of residual tissue damage is simply the difference between the latter and the former. It is clear from this plot that the ratio of the depth of residual tissue damage to the recession depth is decreased by operating at the higher fluences.

The results of these preliminary single-pulse calculations have led us to the following conclusions:

The most effective tissue cutting with minimal residual thermal energy and, hence, minimal residual thermal damage, appears to be best achieved by operating with pulses $\leq 10^{-4}s$ in duration and at pulse fluences $\geq 30 \text{ J/cm}^2$, or, with peak pulse irradiances $\geq 300 \text{ kW/cm}^2$. Under these



A-3051

Figure 2-8. Calculated tissue recession depth and thermal damage depth (relative to original surface) as a function of pulse fluence for several different pulse durations.

conditions, tissue recession velocities are predicted to be so rapid that the recession front literally keeps up with the thermal wave front and, as a result, inhibits the deposition of heat beneath the receding surface.

Analytical Blow-Off Model

One simple thermal model of pulsed laser ablation which is occasionally employed is a critical energy "blow-off" model based on Beer's law. This model assumes the laser energy fluence is deposited in depth according to Beer's law, i.e., $F(Z) \sim F_0 e^{-Z/\delta}$ (where δ is the $(1/e)$ absorption depth at the laser wavelength), and that the target material is ablated to a depth at which the deposited energy just falls below a critical energy density required for ablation. Because it neglects thermal conduction, this model can only be applied to short pulse exposures for which $t_p \leq \delta^2/\kappa$, where κ is the thermal diffusivity of the target material. For example, for tissue interactions at CO_2 wavelengths ($\lambda = 10.6$ microns, $\delta = 1.3 \times 10^{-3}$ cm), this would correspond to pulse durations $\leq 10^{-3}$ seconds. The above assumptions lead to the following relationships:

$$-\left. \frac{\partial F}{\partial Z} \right|_{Z=Z_r} = \epsilon_c = (1-R) F_0 / \delta e^{-Z_r/\delta} \quad (3)$$

$$F_T = \delta \epsilon_c / (1-R) \quad (4)$$

$$Z_r = \delta \ln(F_0/F_T) \quad (5)$$

and

$$Q_{\text{residual}} = F_T$$

where

$$\begin{aligned} \epsilon_c &= \text{critical energy density for ablation (J/cc)} \\ &= \rho h_{\text{abl}} = \rho(h_v + C(T_v - T_0)) \end{aligned}$$

$$Z_r = \text{material recession or "blow-off" depth}$$

$$R = \text{target reflectance}$$

$$F_T = \text{threshold fluence for ablation (J/cm}^2\text{)}$$

Q_{residual} = thermal energy remaining in target after ablation ends
(J/cm²).

For tissue (water), h_v is taken to be 2257 J/g, $C = 4$ J/g°C, $T_v = 100^\circ\text{C}$, and $T_0 = 37^\circ\text{C}$. This gives $h_{\text{abl}} = 2.6$ kJ/g.

Below, we apply this model to the pulsed tissue ablation experiments of Walsh et al. and compare the results to corresponding predictions of the numerical heat conduction model.

Comparisons with Data

The only tissue ablation data we found that could reasonably be used to assess single-pulse tissue response is the data of Walsh et al.,⁸ recently obtained at the Wellman Laboratory, Massachusetts General Hospital. In those experiments, the ablation and residual damage of pig skin was studied using 2- μs long pulses from a CO₂ TEA laser. A 1.6 \times 2.0 mm spot size was used in all experiments. The residual tissue damage was assessed from laser exposures performed in vivo, after which the irradiated site was biopsied and the tissue processed for histological examination. Mass removal rates, on the other hand, were measured in vitro by mounting a sample of pig skin on an electronic balance and recording the weight loss resulting from laser exposure using a computer-controlled data acquisition system.

Walsh's observations of mass loss are presented in Figure 2.9. The single-pulse mass loss is inferred in these experiments by accumulating a train of pulses on one tissue sample at a low repetition rate (approximately 2 Hz), measuring the accumulated mass loss, and effectively dividing by the number of pulses. The number of pulses delivered varied from 40 at high fluences to 130 at the lowest fluence. Plotted in Figure 2.9 is the average mass ablated per pulse per unit area versus the average incident fluence per pulse (J/cm²/pulse).

Also plotted with the data are corresponding single-pulse predictions of the one-dimensional heat conduction code (solid curves) and the predictions of the Beer's law blow-off model (dashed curves) for two different assumed values

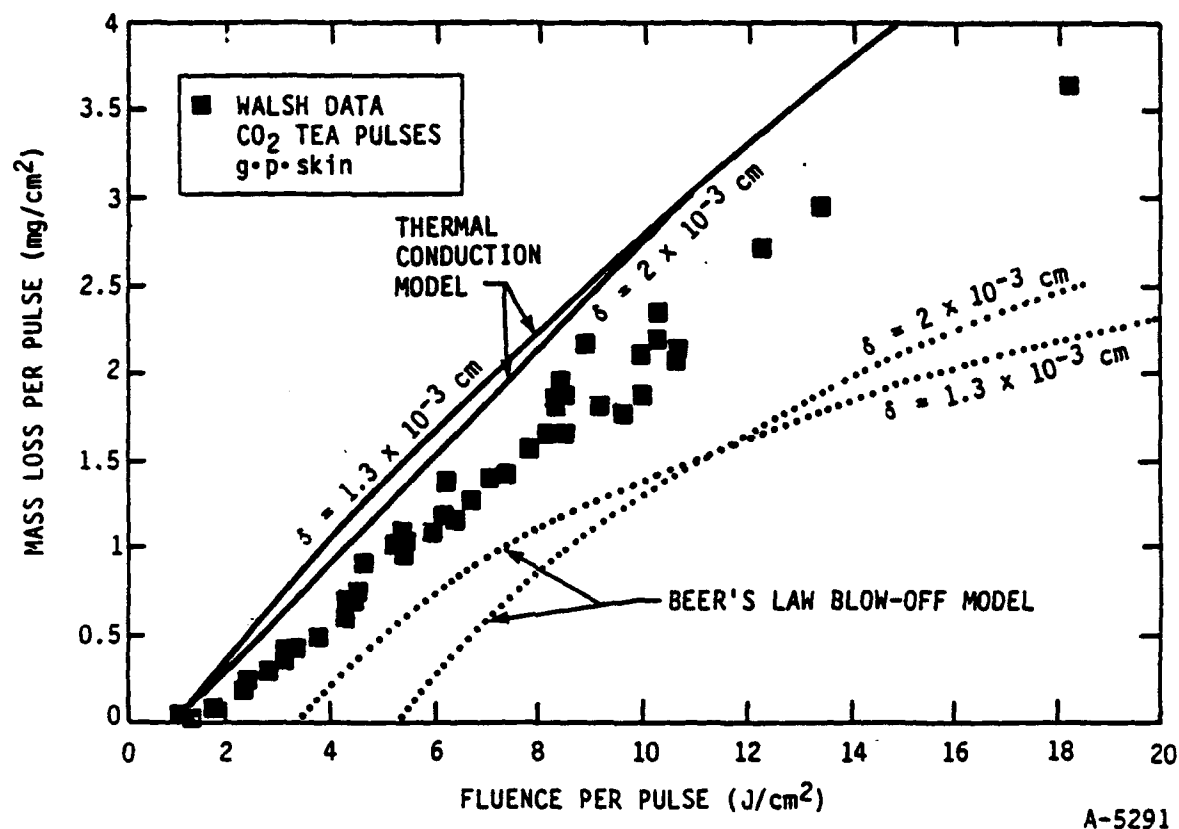


Figure 2-9. Model/data comparisons of tissue mass loss per pulse versus fluence per pulse for irradiation by micro-second duration CO₂ TEA laser pulses.

of the absorption depth. The $(1/e)$ absorption depth previously used in the thermal conduction calculations was 13 microns. The calculated areal mass loss is related to recession depth simply as $\Delta m = \rho Z_r$ where ρ is the tissue density (1.05 g/cc used).

There are several significant features of the results shown in Figure 2.9 that are worth noting. Perhaps the most important feature is that the observed dependence of the mass loss on pulse fluence appears to be more linear than logarithmic and, therefore, fails to follow the predictions of a blow-off model. Even if a shorter absorption depth or lower critical energy for vaporization were arbitrarily assumed to better fit the data at the lower fluences, there would then be an even larger discrepancy at the higher fluences (the blow-off model would significantly underpredict the mass loss).

The dependence of the measured mass loss on pulse fluence is clearly in better agreement with that predicted by the thermal conduction model. In

addition, the thermal conduction model much more closely predicts the fluence "threshold" at which measurable ablation is observed ($\sim 1 \text{ J/cm}^2$). The only significant discrepancy between the predictions of the thermal conduction calculations and the data is that the measured mass loss is generally about 20 to 25 percent lower than the predictions. We offer a possible explanation for this discrepancy at the conclusion of this discussion.

This apparent linear dependence of mass loss on pulse fluence suggests that, at least for pulse fluences sufficiently above "threshold," a model of "steady state" vaporization is much more appropriate than a critical energy blow-off model. It is also significant that measurable mass loss is observed at a lower fluence than the critical threshold fluence defined in the blow-off model. This is consistent with a thermal conduction and surface vaporization model which allows vaporization to occur as soon as the front surface temperature reaches the boiling point, i.e., $F_{\text{abs}} \approx \rho C(T_B - T_0) \cdot \delta \approx 0.34 \text{ J/cm}^2$ (for $\delta = 13 \text{ }\mu\text{m}$). Subsequent to that point, the mass vaporization rate (and corresponding surface temperature) during the pulse are determined by the absorbed flux rather than explicitly by fluence.

In a similar manner, the assumptions of the blow-off model lead to an overestimate of the residual thermal energy or retained heat in the tissue after ablation terminates. For example, we see from Figure 2.7 that for an incident fluence of 10 J/cm^2 , the thermal conduction model predicts a final residual thermal energy of $\sim 1.2 \text{ J/cm}^2$ while, for the same absorption depth of $13 \text{ }\mu\text{m}$, the blow-off model predicts $\sim 3.3 \text{ J/cm}^2$, or about a factor of 3 higher. Part of the reason for this difference is that in the conduction model some evaporation can continue for a significant time after the laser pulse terminates, allowing the tissue to cool evaporatively and leaving less heat behind, while in the blow-off model no evaporation is permitted after the pulse terminates. In the thermal conduction/surface vaporization model, ablation will continue until the front surface temperature drops to $\sim 100^\circ\text{C}$ (or local incremental energy density $\approx 260 \text{ J/g}$). This is nearly one-tenth of the critical energy density at which vaporization is forced to terminate in the blow-off model.

These differences in the residual thermal energies predicted by the two models also lead to differences in the extent of residual thermal tissue damage that is predicted to occur. To first order, in fact, one would expect the zone of residual damage to scale proportionally with the residual thermal energy. For example, at an incident fluence of 10 J/cm^2 and $\delta = 13 \text{ }\mu\text{m}$, we calculate from the code $Q_r = 1.2 \text{ J/cm}^2$ and a final depth of residual damage of 51 microns. In contrast, if we allow the corresponding higher residual energy of the blow-off model ($Q_r = 3.3 \text{ J/cm}^2$) to conduct into the tissue and calculate the denaturation which results, we find final residual damage depths of between 130 to 160 microns.

The observed depths of residual damage in the Walsh experiments were quoted to be between 50 and 100 microns over the pulse fluence range of 2 to 18 J/cm^2 . For the code calculations carried out over the same fluence range (and for an assumed absorption depth of between 13 and 20 microns), damage depths are found to be between 40 and 80 microns. On the other hand, using the corresponding residual energies given by the blow-off model, damage depths are predicted to be from a minimum of 130 microns to a maximum of 240 microns. Thus, once again, we find the code predictions to be in closer agreement with the observations.

Finally, we have considered why the measured "single-pulse" mass loss in Walsh's experiments is generally lower than the single-pulse code predictions. At this point we believe the most likely explanation comes from the fact that the experimental "single-pulse" mass loss was obtained by averaging over the mass loss from an accumulation of multiple single-pulse exposures to the same area of tissue. It is therefore quite likely that, in the process, the surface of the tissue became dried out or dessicated, thus leaving less tissue water available for vaporization on subsequent pulses. We suggest that in the future an attempt be made to obtain true "single-pulse" data. In addition, modeling efforts should be directed toward a multicomponent treatment of tissue, i.e., aqueous and non-aqueous components. This would allow for an accounting of the depletion of available tissue water. A proper treatment, however, will require a model for the pyrolysis and possible charring of the non-aqueous residue.

2.4 Summary and Conclusions

Detailed model calculations have been carried out to assess the thermal response and ablation of biological tissue exposed to continuous wave and short pulse CO₂ laser radiation. The models developed, however, are applicable to any laser wavelength for which absorption in tissue dominates over scattering.

The model predictions are shown to be in close agreement with available data on tissue damage and ablation. The results confirm that a transient thermal conduction model that includes an equation for the thermal denaturation of tissue protein and the surface vaporization of tissue water can in large measure explain the experimental observations.

Future modeling improvements that are planned are a multicomponent treatment of tissue that will model the non-aqueous as well as the aqueous components, and the inclusion of a laser source term that accounts for scattering.

2.5 References

1. See, for example, recent issues of the journal Lasers in Surgery and Medicine, or the IEEE Journal of Quantum Electronics Special Issue on Lasers in Biology in Medicine, Vol. QE-20 (December 1984).
2. A.J. Walsh, "The Thermal Response of Laser Irradiated Tissue," IEEE J.Q.E., Vol. QE-20, pp. 1741-1481 (December 1984).
3. M.L. Wohlbarsht, "Laser Surgery: CO₂ or HF," IEEE J.Q.E., Vol. QE-20, pp. 1427-1432 (December 1984).
4. G. Delfino, et al., "Induced Modifications and Temperature Rises in the Laser Irradiation of Whole Biological Specimens in Vivo," IEEE J.Q.E., Vol. QE-20, pp. 1489-1496 (December 1984).
5. F. Partovi, et al., "A Model for Thermal Ablation of Biological Tissue Using Laser Radiation," to be published in Lasers in Surgery and Medicine.
6. L.A. Popper and N.H. Kemp, "User Manual for PSI Codes for Calculating Laser Effects," Physical Sciences Inc., Technical Report TR-396 (October 1983).

7. A.N. Takata, L. Zaneveld, and W. Richter, "Laser-Induced Thermal Damage in Skin," USAF School of Aerospace Medicine, Brooks AFB, TX, Report SAM-TR-77-38 (1977).
8. J.T. Walsh, Jr., T.F. Deutsch, T. Flotte, M.R. Prince, and R.A. Anderson, "Comparison of Tissue Ablation by Pulsed CO₂ and Excimer Lasers," Paper presented to Conference on Lasers and Electrooptics (CLEO), San Francisco, CA (June 1986).
9. F.C. Henriques, "Studies of Thermal Injury," Arch. Pathol. 43, 489 (1947).
10. A.M. Stoll and L.C. Green, "Relationship Between Pain and Tissue Damage Due to Thermal Radiation," J. Appl. Physiol. 14, 373 (1959).
11. A.J. Welch and G. Polhamus, "Measurement and Prediction of Thermal Damage in the Retina of the Rhesus Monkey," IEEE Trns. Biomed. Eng. BME-31, 633 (1984).
12. A.N. Takata, "Development of Criteria for Skin Burns," Aerospace Med. 45, 634 (1974).
13. T. Halldörson, J. Langerholc, "Thermodynamic Analysis of Laser Irradiation of Biological Tissue," Appl. Opt. 17, 3948 (1978).
14. CRC Handbook of Chemistry and Physics.
15. C.J. Knight, AIAA Journal 17, 519 (1979).
16. F.W. Dabby, and U.C. Pack, IEEE J. Quant. Elect. QE-8, 106 (1972).
17. G. Laufer, "Primary and Secondary Damage to Biological Tissue Induced by Laser Radiation," Appl. Opt. 22, 676 (1983).
18. M.S. Baggish and M.M. Elbakry, "Comparison of Electronically Superpulsed and Continuous-Wave CO₂ Laser on the Rat Uterine Horn," Fertility and Sterility 45, 120 (1986).
19. L.I. Deckelbaum, J.M. Isner, R.F. Donaldson, S.M. Laliberte, R.H. Clarke, and D.N. Salem, "Use of Pulsed Energy Delivery to Maximize Tissue Injury Resulting from Carbon Dioxide Laser Irradiation of Cardiovascular Tissues," JACC 7, 8898 (1986).

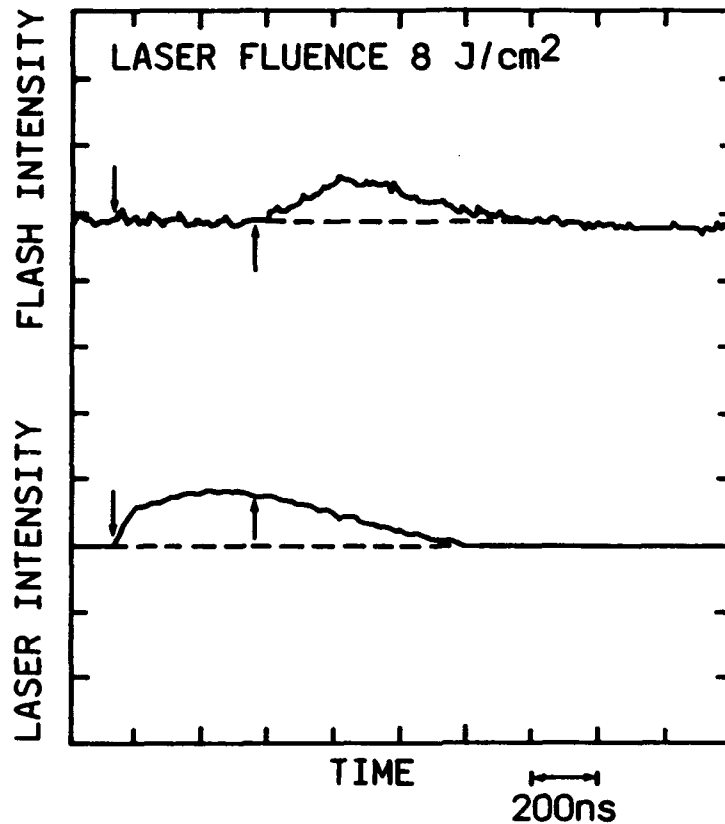
3. PLASMA MODELING

Experiments on laser-induced fragmentation of biliary and urinary calculi have shown that fragmentation is always accompanied by plasma formation^{1,2}. The plasma is visible as a bright flash of duration of the order of the pulse length. Spectroscopic investigation of the radiation emitted by biliary calculi during the flash has shown that the emission consists of a continuum spanning the visible spectrum with strong lines of ionized Calcium appearing in absorption². The continuum disappears at a later time and the lines then appear as emission features.

We have investigated mechanisms consistent with the experimental data through which a plasma could be ignited in the calculi. The data indicate that the threshold is determined primarily by the laser fluence rather than by the laser irradiance. Graham Watson¹ performed experiments using various lasers with pulse lengths extending from 20 ns (Q switched ruby and Nd Yag lasers) to 300 μ s (flash lamp pumped dye laser). He quotes at the shortest pulse length a threshold of 40 mJ at the doubled Yag frequency ($\lambda = 0.53 \mu$ m) with a beam diameter at focus of 0.5 mm. This corresponds to a fluence $\phi = 40 \times 10^{-3} / (\pi \times (0.05)^2 / 4) = 20 \text{ J/cm}^2$. This number is to be compared with a fluence of 34 J/cm^2 at the longest pulse length studied, $\tau = 300 \mu$ s, corresponding to the conditions $\lambda = 0.577 \mu$ m, $d = 1 \text{ mm}$. The threshold irradiances, however, varied over several orders of magnitude ($I = 10^9 \text{ W/cm}^2$ for $\tau = 20 \text{ ns}$ and $I = 10^5 \text{ W/cm}^2$ for $\tau = 300 \mu$ s). The fluence thresholds, which are found to lie in the range $4 - 40 \text{ J/cm}^2$, appear also to be relatively insensitive to laser wavelength.

Figure 3.1 shows plasma flash data taken by Teng et al² who used a dye laser ($\lambda = 690 \text{ nm}$, $\tau = 0.8 \mu$ s) on a pigmented biliary calculus. This figure shows that breakdown has occurred within 400 ns after the beginning of the pulse and that, at the onset of breakdown, 5 J/cm^2 have been deposited in the stone. The beam irradiance is estimated to be $I = 8 \text{ J/cm}^2 / 600 \text{ ns} = 10^7 \text{ W/cm}^2$.

Laser-induced breakdown in semi-transparent optical materials has been studied in great detail³. The threshold irradiances in pure crystalline



A-7947

Figure 3.1. Time dependence of laser and flash intensities. Arrows mark the beginning of the laser pulse and of plasma emission (from Teng et al²).

materials devoid of impurities and defects are expected to be quite high, in excess of 10^{10} W/cm². These thresholds are much higher than those that have been observed for the breakup of stones. Much lower breakdown thresholds have been observed in optical materials due to surface or bulk defects. The surface defects can be cracks, grooves, or spherical pores⁴. There may also be dust particles or surface inclusions. Bulk impurities could be platinum particles from the crucibles used in the fabrication process. In a similar fashion, absorbing inclusions in biliary calculi would come from the presence of pigment. Absorption sites will result in localized heating that under certain conditions can lead to thermal runaway.

It seems apparent, from the low irradiance thresholds observed for breakdown on gall stones and urinary tract calculi, that plasma ignition is associated with absorption and ignition on localized sites. The stones have long absorption lengths in the visible which means that the radiation can penetrate

deeply. At the breakdown fluences of tens of joules per square centimeter, one does not expect sufficient bulk heating to account for the phenomena observed. What we believe is happening is that the temperature around the absorption site is high enough to trigger non-linear absorption in the surrounding medium. If this absorption is high enough, the added heating will lead to thermal runaway. There will be a threshold irradiance associated with the minimum temperature to initiate the runaway and a threshold fluence associated with the development of individual plasmas at each site and coalescence of the plasmas. Plasmas will radiate in the UV and deep UV. Absorption of these high-energy photons by the calculus will cause ionization of the surrounding medium. Inverse Bremsstrahlung absorption by the electrons thus generated will result in enhanced absorption and provides a mechanism for plasma growth.

Absorption by inclusions of various sizes has been analyzed by Sparks and Duthler⁵. These authors considered temperature rises of only 1000 K, since they were solely concerned with material failure due to stress buildup. Anisimov and Makshantsev also considered absorption by inclusions and postulated a thermally-dependent absorption coefficient of the medium of the form⁶:

$$k = b \exp - (E/T) \quad (1)$$

where E is an energy of the order of the band gap of the material. They were able to calculate the threshold irradiance as a function of the particle size. We review their theory below.

Theory of Anisimov and Makshantsev.

Let there be an absorbing inclusion of radius R, embedded in a non-absorbing medium. After a transient period, a steady state temperature profile will be established in which the flow of heat out of the inclusion balances the power absorbed from the laser field. If we assume a spherically symmetric temperature profile, then the heat conduction equation in the surrounding medium can be written as

$$\frac{1}{r^2} \frac{d}{dr} \left(r^2 K \frac{dT}{dr} \right) = 0 \quad (2)$$

subject to the boundary condition $T = T_\infty$ when $r \rightarrow \infty$ and, at $r = R$,

$$\begin{aligned} -K \frac{dT}{dr} &= \frac{1}{4\pi R^2} (\pi R^2 Q_{\text{abs}} I) = \\ &= \frac{Q_{\text{abs}}}{4} I \end{aligned} \quad (3)$$

where I is the laser irradiance, K the thermal conductivity, and Q_{abs} the absorption efficiency of the inclusion. The solution to Eqs. (2) and (3), assuming that K is independent of T , is:

$$T - T_\infty = \frac{Q_{\text{abs}} I R^2}{4Kr} \quad (4)$$

Anisimov and Makshantsev assume that the medium surrounding the inclusion has a temperature-dependent absorption coefficient of the form given by Eq. (1). Such a form is reasonable if one assumes that a) free or bound electronic states can be thermally populated into allowed states having energy E above the Fermi level and b) the electrons in these states can absorb the laser photons. Because of this extra absorption, the temperature will rise above the solution given by Eq. (4). In order to calculate this temperature rise, one must solve the time-dependent heat equation:

$$\rho C \frac{\partial T}{\partial t} = \frac{1}{r^2} \frac{\partial}{\partial r} \left(r^2 K \frac{\partial T}{\partial r} \right) + kI \quad (5)$$

where ρ and C are the density and specific heat of the material. A solution to (5) can be obtained by expanding around the time-independent solution $T_0(r)$ which is approximated by Eq. (4) (since k is assumed small)

$$T(t) = T_0(r) + \theta(t, r)$$

and writing that

$$k(T) = k(T_0) + \frac{dk}{dT} \theta = k(T_0) + k' \theta .$$

We expand θ as follows

$$\theta(t) = \sum_{\gamma} c_{\gamma} e^{-\gamma t} \Psi_{\gamma}(r) . \quad (6)$$

Inserting the expansion (6) into Eq. (5), one finds that each Ψ_{γ} should satisfy

$$\frac{1}{r^2} \frac{\partial}{\partial r} (r^2 \Psi_{\gamma}) + \Psi_{\gamma} (\bar{\gamma} + V(r)) = 0 \quad (7)$$

where

$$\bar{\gamma} = \frac{\rho C \gamma}{K}$$

and

$$V(r) = \frac{I}{K} k'$$

Anisimov and Makshantsev seek a solution to Eq. (7) with the boundary conditions

$$\Psi_{\gamma} \rightarrow 0 \text{ when } r \rightarrow \infty \text{ and } \left. \frac{d\Psi}{dr} \right|_R = 0 ,$$

the latter condition meaning that the additional heat absorption by the medium surrounding the inclusion does not affect the heat flow out of the inclusion (which is just the power absorbed by the inclusion from the laser beam). If a solution to Eq. (7) can be found, that admits a negative eigenvalue γ (or $\bar{\gamma}$), then, following Eq. (6), one sees that there will be a thermal runaway. Using the fact that $V(r)$ is appreciably different from zero only in the immediate vicinity of R , they find, by integrating Eq. (7) over r once and using the boundary condition on Ψ , that a solution with negative γ can exist only if the following condition on k is satisfied.

$$\int_R^{\infty} k' dr > \frac{K}{IR} \quad (8)$$

Now,

$$\int_R^{\infty} k' dr = \int_{T(R)}^T \frac{dk}{dT} \left(\frac{dr}{dT} \right) dT \approx k[T_0(R)] \left(\frac{dT}{dr} \right)^{-1}_{r=R}$$

If we now use Eq. (3) to calculate $K(dT/dr)_R$, we can recast Inequality (8) as follows:

$$k(T_0) > \frac{Q_{abs}}{4R}$$

or, using Eq. (4) for $(T_0 - T_\infty)$,

$$I > \frac{4K}{RQ_{abs}} \left[\frac{E}{\ln \left(\frac{4Rb}{Q_{abs}} \right)} - T_\infty \right] \quad (9)$$

Equation (9) is the fundamental result of Anisimov and Makshantsev. It differs slightly from their Eq. (8) in which they dropped the T_∞ term and where, due to a misprint, the logarithm term appeared in the numerator instead of the denominator. Also, rather than using Q_{abs} , they defined an absorption factor α ($\approx Q_{abs}/4$).

Discussion

Inequality (9) shows the breakdown threshold irradiance scales roughly as R^{-1} . There will be a whole range of sizes for the defects in the focal volume and the larger ones will be the most easy to break down. In a given experiment, the irradiance I is specified; therefore, one can expect that all inclusions whose radius exceeds a threshold value corresponding to Eq. (9), being satisfied, will be a plasma ignition site. In order to test whether the theory of Anisimov and Makshantsev is consistent with the experimental data, we must a) show that Inequality (9) allows low threshold irradiance and b) explain why there is also an important effect of fluence. As a typical example, let us set $E = 60,000$ K corresponding to a band gap of 5.5 eV, $Q_{abs} = 0.5$, $K = 10^{-2}$ W/cmK and a limiting high temperature absorption coefficient $k = 10^5$ cm $^{-1}$ (i.e., $b \approx 10^5$). We find that for $R = 1$ μ m, $I = 2 \times 10^7$ W/cm 2 , while for $R = 10$ μ m, $I = 7 \times 10^5$ W/cm 2 . These thresholds are not unreasonable.

The fact that there is also a threshold fluence that is weakly dependent on pulse length can arise from two phenomena. First, one must deposit enough energy in the inclusion for the steady state profile to be established. Second, the plasmas, once ignited, require a certain time to grow and coalesce.

Estimate of Laser Ignition Time and Threshold Fluence

We can obtain a rough estimate of the heating time by looking at the energy balance equation. The heating curve is shown in Figure 3.2. There is an initial transient that lasts a time τ_H during which the temperature of the inclusion rises linearly with time. After this time, the rate of temperature rise decreases, the temperature asymptoting to a steady state value T_s . The departure from the linear behavior occurs when the thermal diffusion length into the surrounding medium, ℓ_D , becomes comparable to the radius of the inclusion

$$\ell_D = \sqrt{\chi t_H} \approx 0.2 \text{ to } 0.5 \times R$$

where χ is the thermal diffusivity and t_H the thermal diffusion time. The thermal runaway that was discussed in the previous paragraphs can occur under two different regimes, depending on the irradiance level. If $\gamma t_H \gg 1$, then thermal runaway occurs during the rising portion of the temperature versus

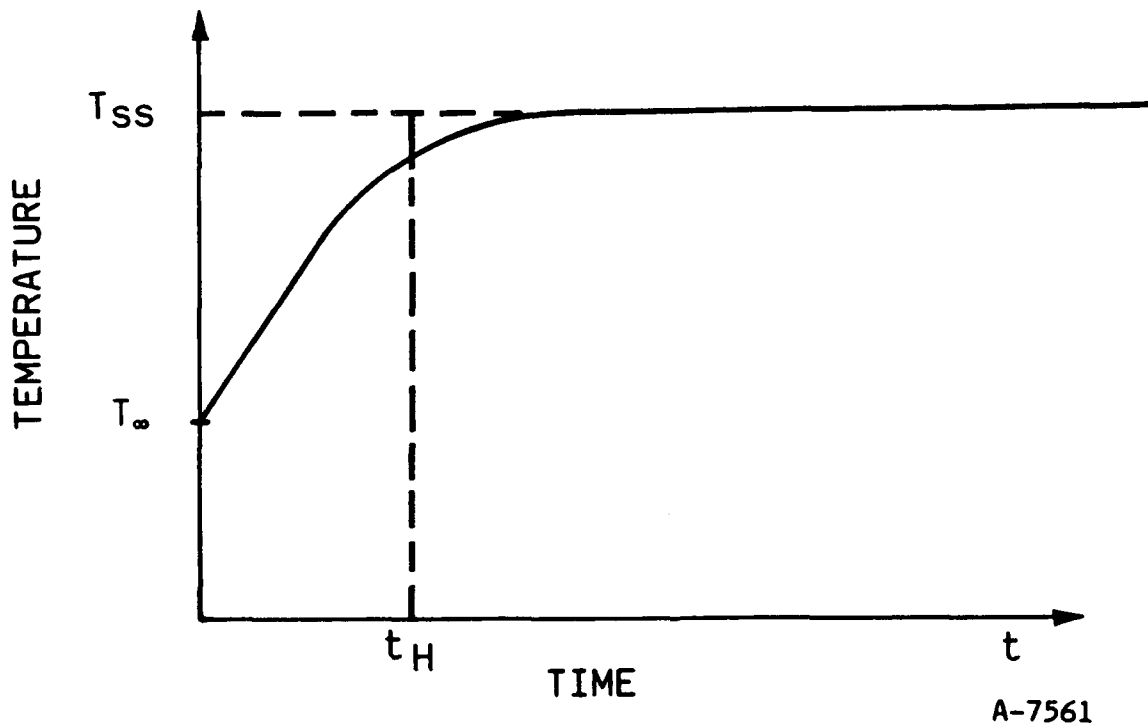


Figure 3.2. Temperature versus time at the surface of an absorbing inclusion.

time curve, i.e., breakdown is initiated before the particle temperature can attain a steady state. In the opposite limit, $\gamma t_H < 1$, thermal runaway will occur long after steady state heating has been achieved. Due to the strong temperature dependence of k on T (see Eq. (1)), γ will be a strong function of T . It is therefore valid to define a critical temperature T_c that separates the two regimes. A rough estimate of T_c is obtained by setting the non-linear absorption coefficient k , given by Eq. (1), to the absorption coefficient in the inclusion k_i

$$k(T_c) = k_i$$

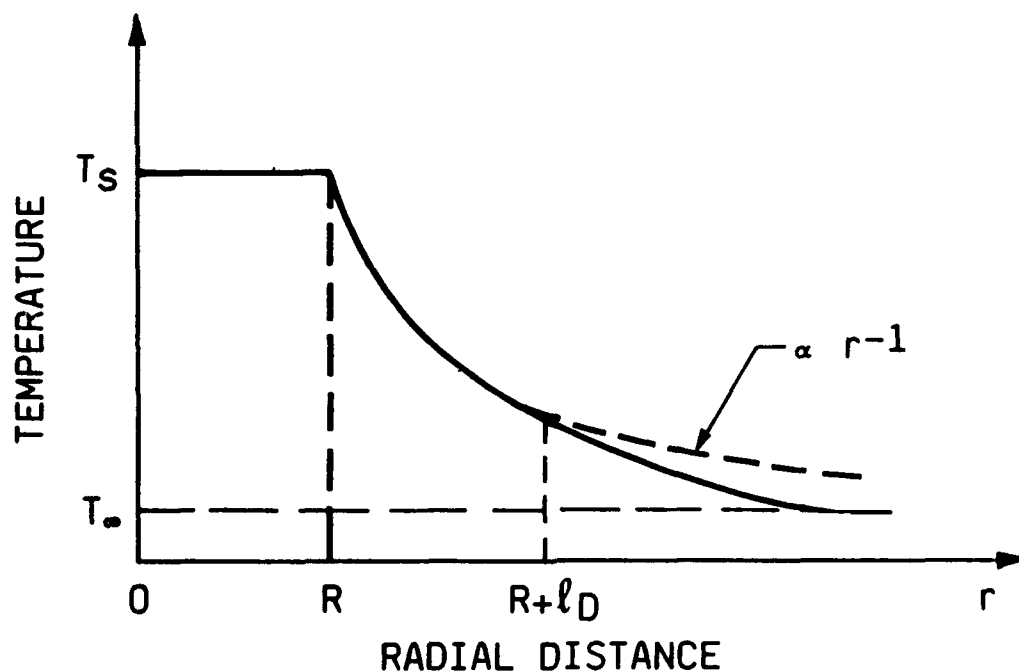
For the purpose of definiteness, in what follows we shall set

$$\Delta T = T_c - T_\infty = 2000 \text{ K}.$$

If, as we shall assume, the inclusion has a large thermal conductivity as compared to the surrounding medium, then the temperature profile during the transient is as shown in Figure 3.3. $T = T_s$ for $r < R$,

$$T = (T_s - T_\infty) \frac{R}{r} + T_\infty \quad R < r < R + \ell_D$$

and T drops rapidly to T_∞ when $r > R + \ell_D$. The thermal energy corresponding



A-7562

Figure 3.3. Temperature profile during heating stage.

to this profile is

$$E = \rho_1 C_1 \Delta T \int_0^R 4\pi r^2 dr + \rho_2 C_2 \Delta T \int_R^{R+\ell_D} 4\pi r^2 \left(\frac{R}{r}\right) dr$$

$$= \frac{4\pi}{3} R^3 \rho_1 C_1 \Delta T \left[1 + \frac{3}{2} \frac{\rho_2 C_2}{\rho_1 C_1} \left[\left(1 + \ell_D/R\right)^2 - 1 \right] \right]$$

where the subscripts 1 and 2 refer to the inclusion and to the calculus material. Equating E with the energy absorbed from the laser beam, we find:

$$\phi = \int^t I dt' = \frac{4}{Q_{abs}(R)} R \rho_1 C_1 \Delta T \left\{ 1 + \frac{3}{2} \frac{\rho_2 C_2}{\rho_1 C_1} \left[\left(1 + \sqrt{\chi t}/R\right)^2 - 1 \right] \right\}$$

We set $Q_{abs} = 1$ for a strongly absorbing inclusion larger than the wavelength and $Q_{abs}(R) = (2/3)k_i R$ for a weakly absorbing inclusion ($k_i R < 1$). We show in Figures 3.4 and 3.5 the fluences for plasma ignition as a function of inclusion radius for a set of pulse lengths. The conditions assumed for the calculations were $\rho_1 = \rho_2 = 2.2 \text{ g/cm}^3$, $C_1 = C_2 = 1.5 \text{ J / (gK)}$, $\chi = 10^{-2} \text{ cm}^2 \text{ s}^{-1}$ and $\Delta T = 2000 \text{ K}$.

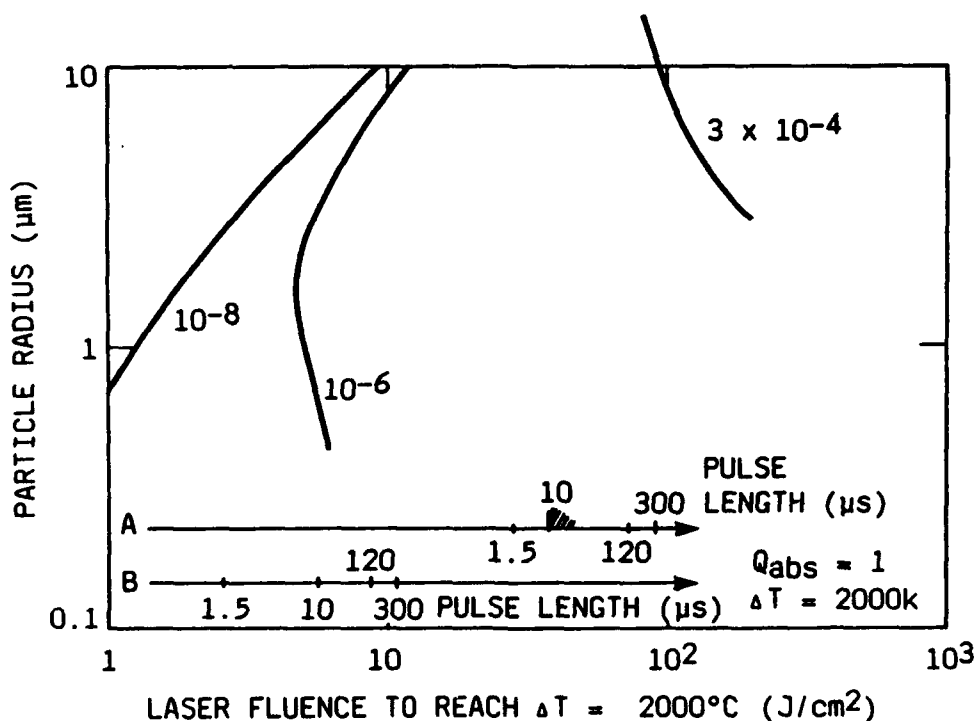


Figure 3.4. Laser fluence to reach $\Delta T = 2000 \text{ K}$, strongly absorbing particle ($Q_{abs} = 1$).

A-7943

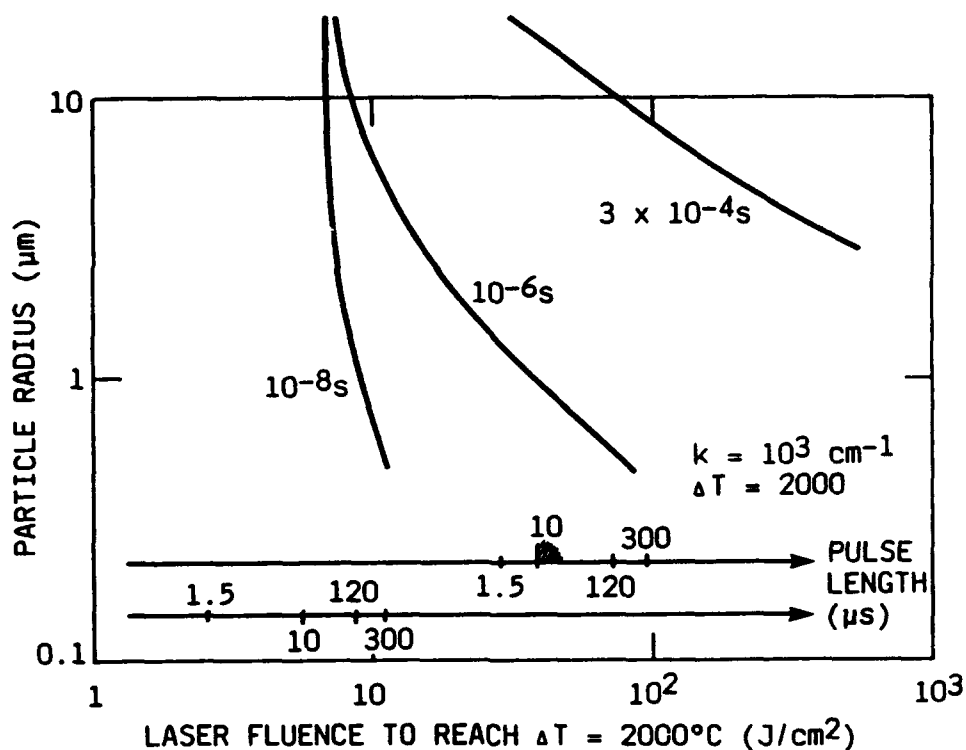
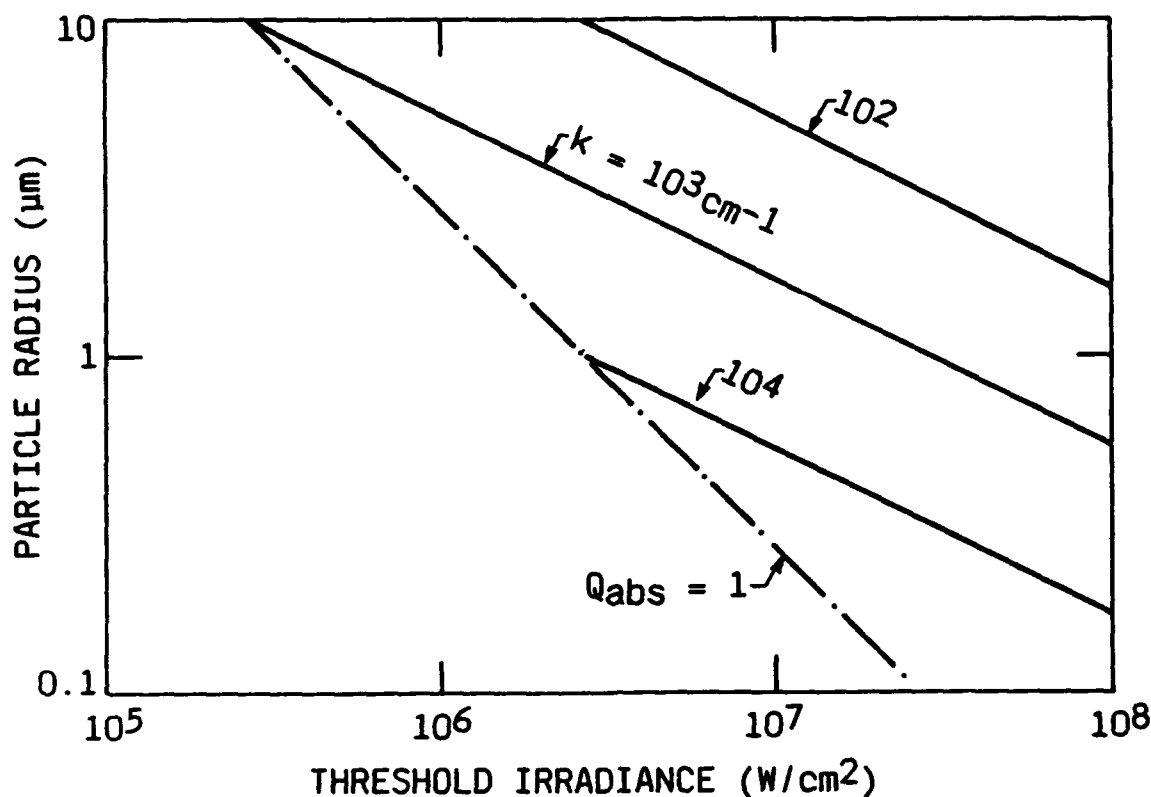


Figure 3.5. Laser fluence to reach $\Delta T = 2000$ K, weakly absorbing particle ($k = 10^3 \text{ cm}^{-1}$).

One sees a very different behavior of threshold with particle radius at $\tau_p = 3 \times 10^{-4} \text{ s}$ than at the two shorter pulse lengths considered. The thermal diffusion depth is, in general, much larger ($\ell_D \approx 20 \mu\text{m}$) than the particle radius when $\tau_p = 3 \times 10^{-4} \text{ s}$, so that the volume heated is much larger than the inclusion. The threshold fluence will, under such conditions, vary inversely with the power absorbed by the inclusion. The power absorbed varies as $\pi R^2 Q_{\text{abs}}$, thus leading to an R^{-2} (kR^{-3}) dependence for strongly (weakly) absorbing inclusions. If, however, $\ell_D \leq R$, as in the case of the two shorter pulse lengths considered, the threshold fluence will vary as $R / Q_{\text{abs}}(R)$ (see Eq. (10)), i.e., as R for the strongly absorbing inclusions and will be independent of inclusion radius for the weakly absorbing inclusions. The threshold irradiance versus particle size is shown in Figure 3.6 for a series of absorption coefficients.

It is of interest to compare our results with experimentally observed thresholds on calculi. We have done this by introducing extra abscissas in Figures 3.4 and 3.5, corresponding to experimentally observed breakdown fluences observed at the pulse lengths indicated. All the data were taken



A-7555

Figure 3.6. Threshold irradiance versus particle radius.

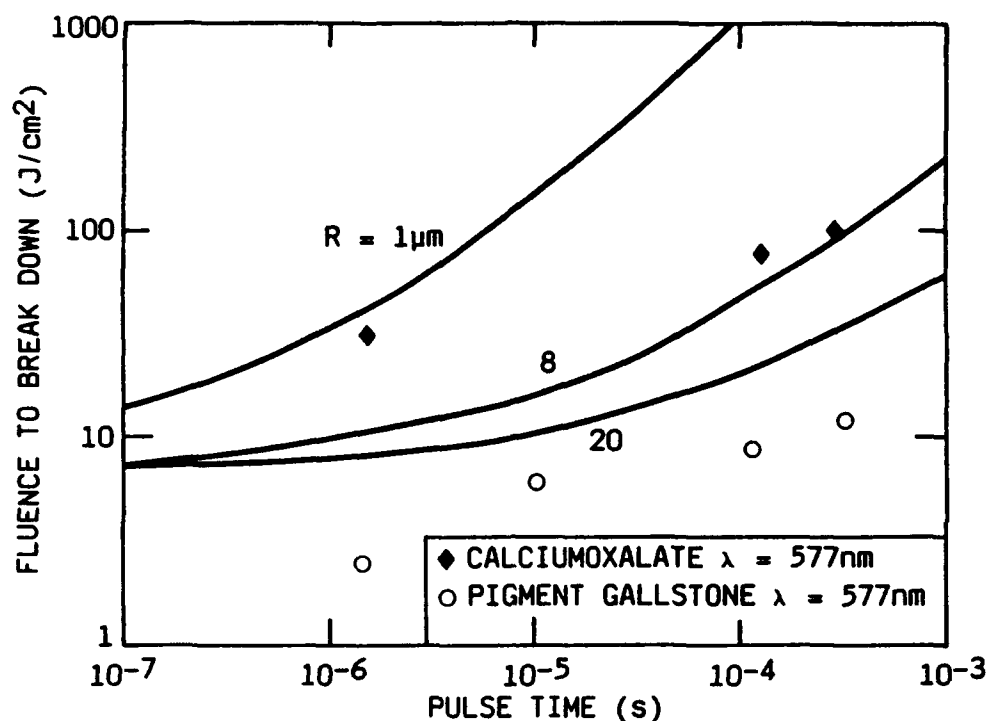
from the thesis of Watson¹. In comparing the data with the theory, one must keep in mind that experimental thresholds probably include an additional fluence for plasma growth. The threshold data on axis A were for uncolored calcium oxalate calculi at $\lambda = 577$ nm. The threshold data on axis B, taken at the same wavelength, were for a dark pigmented gallstone. The thresholds for B are approximately one order of magnitude lower than for A.

Note that Teng et al have also measured laser-induced fragmentation thresholds of biliary calculi at $\lambda = 690$ nm and with $\tau_p = 0.8$ ns. From Figure 3.1 we see that their threshold is ≈ 4 J/cm², with plasma being formed at $t = 0.4$ μ s. If we take into account that their fiber diameter (0.3 mm) was one half the fiber diameter of Watson and use the threshold scaling (derived from the data of Watson) $\phi_6 \propto (\text{diameter})^{-1.3}$, we obtain a threshold of 2.4 J/cm² for $\tau = 0.4$ μ s, which is practically the same threshold observed by Watson with $\tau_p = 1.5$ μ s. Because of the slight wavelength dependence of fragmentation threshold observed by Watson, we would expect the threshold at $\lambda = 577$ nm to be less than at 690 nm so that the data of Teng et al and Watson are consistent with each other.

Comparison of our theoretical results with experiments can be made as follows. For the strongly pigmented gallstone, the data indicate a factor of 5 increase in fluence threshold as one goes from $\tau_p = 1.5$ to 300 μs . Such a spread in threshold is consistent with an inclusion radius of 20 μm , for $k \geq 10^3 \text{ cm}^{-1}$ (see Figures 3.5 and 3.4). The observed thresholds, however, are two to four times smaller than the calculated ones. A decrease in the temperature rise by a factor of three, i.e., $\Delta T = 700^\circ\text{K}$ rather than $\Delta T = 2000 \text{ K}$, or an increase in k by a factor of three would bring the results in better agreement. The data for the calcium oxalate stone show practically the same spread in thresholds, but threshold values that are a factor of 4 larger than the model prediction for $R = 20 \mu\text{m}$ and $k = 10^3 \text{ cm}^{-1}$. Agreement between the model and the data can be achieved in this case by decreasing the absorption coefficient by a factor of 4. Though the factor of ten increase in thresholds as one goes from a dark pigmented gallstone to a clear calcium oxalate urinary tract calculus can be explained by a difference in k , the expected lower densities of absorption sites in the clear calculus should also play a role. Effective fragmentation requires a pressure build-up over the whole irradiated surface, which requires that the plasmas ignited at the various sites will be larger in the stones that have fewer ignition sites.

We show in Figure 3.7 the variation of breakdown fluence with pulse length. Calculations were performed for inclusions of radius 1, 8 and 20 μm . The data points have a slope that is consistent with breakdown initiated on inclusions of radius 20 μm , excepting for the pigment gallstone data point at $\tau_p = 1.5 \mu\text{s}$ which is a factor of 2 too low.

We conclude that with a proper (but reasonable) choice of the parameters in the model, agreement can be achieved between the model and the data. The data indicate that plasma ignition is caused by absorbing inclusions of radius 20 μm or larger. Validation of the model will require a) better estimates of the physical properties of calculi, b) evaluation of ΔT , i.e., determination of the temperature dependence of absorption coefficient in the bulk material, and c) determination of the absorptive properties and size distribution of inclusions in the various stones.



A-7944

Figure 3.7. Variation of breakdown fluence with pulse length.

Continuing Work

The rough calculations performed above indicate that plasma ignition in calculi may be due to localized heating at absorbing sites of radius 10-20 μm . It remains to be shown that thermal instabilities can lead to plasma growth and overlap over the time scales of the experiments in which plasmas and stone shattering have been observed. Continuing work will involve solving the heat conduction equation numerically. A steady state temperature profile corresponding to Eq. (4) will be assumed initially. Non-linear absorption with the absorption coefficient of the form $k = b \exp(-E/T)$ will be assumed and introduced into the heat source term. Estimate of the coefficients b and E will have to be obtained from the literature.

Analysis of Laser Produced Plasmas

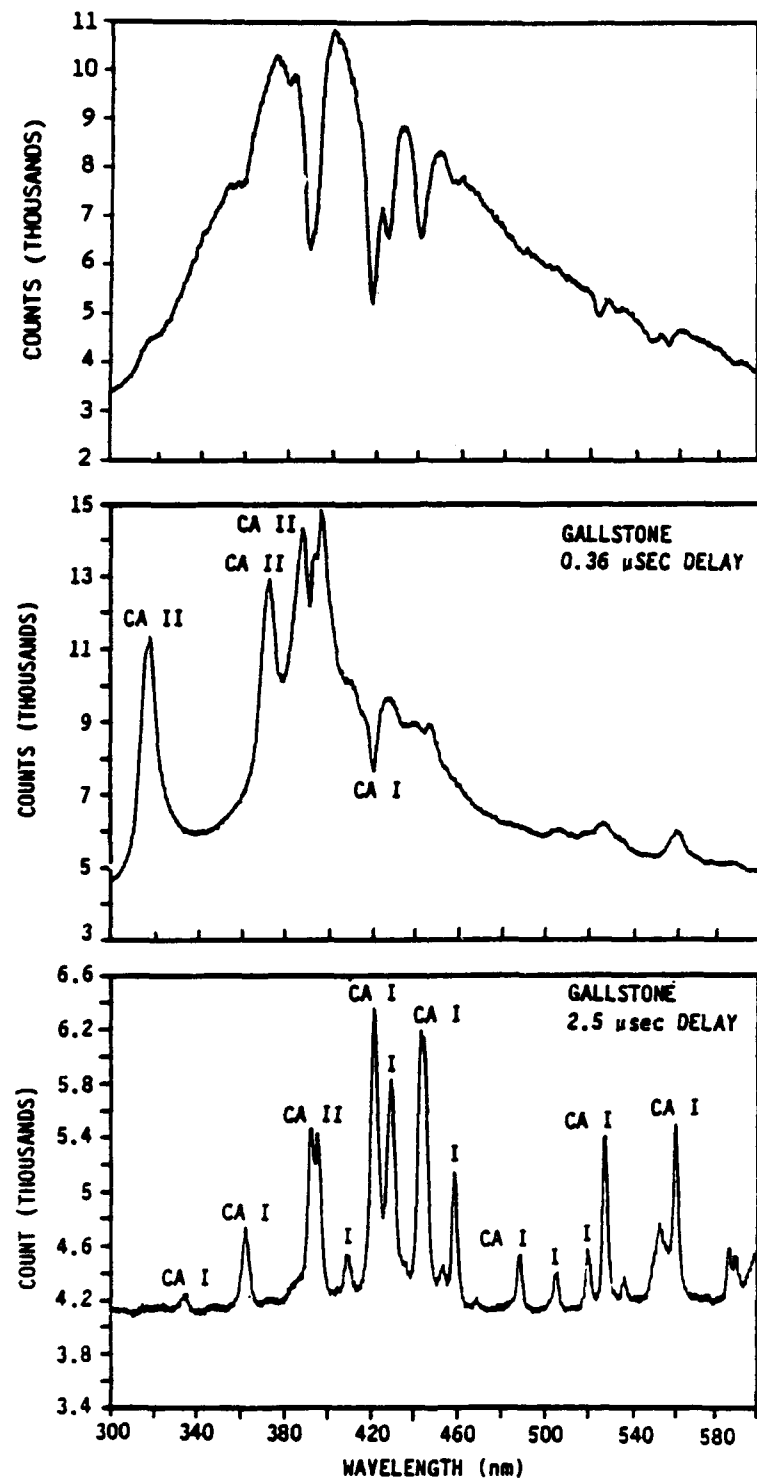
Teng et al² have obtained spectral data of plasmas generated during laser interaction with gallstones and kidney stones. We have analyzed these spectra with the aim of determining time evolution of plasma density, temperature and

pressure. We reproduce in Figure 3.8 the spectra of plasma ignited above biliary calculi 0.22, 0.36 and 1.6 μs after the beginning of the laser pulse. The laser pulse duration was 0.8 μs and fluence 55 J/cm^2 . The first two spectra correspond to plasma radiation during the laser pulse, while the last spectrum was taken 0.8 μs after the end of the pulse. Figure 3.8a shows a continuum with lines of Ca and Ca^+ appearing in absorption. Figures 3.8b and 3.8c also show almost exclusively lines of Ca and Ca^+ in emission. The principal lines of calcium that can radiate in the 300-700 nm range are shown in Table 3.1.

Plasma density can be obtained by looking at the Stark broadening of the spectral lines. Plasma temperature can be obtained by taking the ratio of lines having the same upper state or by comparing the intensities of lines of Ca and Ca^+ in order to determine the ratio of ion to neutral populations. The line strength for a transition from an upper state u to a lower state l will vary as follows:

$$S_{ul} \propto g_u N A_{ul} \exp -(E_u/kT)$$

where A_{ul} is the Einstein coefficient for spontaneous emission, g_u the degeneracy of the upper state, E_u the energy of the upper state, and N the number density of radiating atoms/ions. The values of g , A and E for the principal lines of Ca and Ca^+ are shown in Table 3.1. The temperature can also be obtained from Figure 3.8a by comparing the spectrum to a black body, assuming that the radiation is black in the long wavelength part of the spectrum. If we can assume thermal equilibrium, then the concentration of Ca, Ca^+ , Ca^{++} can be obtained by solving the set of Saha equations for these species. Note that Ca^{++} is Argon-like and will not produce line radiation in the visible part of the spectrum. We show in Figure 3.9 the degree of ionization \bar{z} of Ca as a function of temperature for a series of calcium densities. The densities considered will lead to electron concentrations in excess of 10^{18}cm^{-3} and it is important to take into account the lowering of the ionization potential due to the electric fields surrounding the atoms/

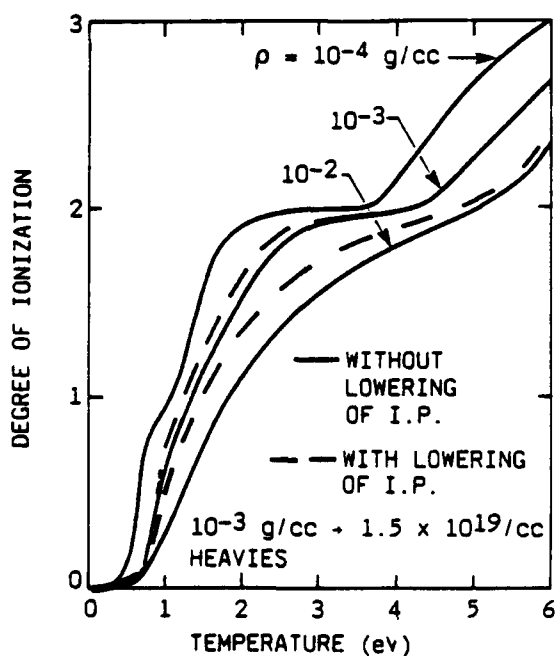


A-7563

Figure 3.8. Spectra of plasma radiation during and after interaction with a biliary calculus. Laser parameters $\tau_p = 0.8 \mu s$, $\phi = 50 J/cm^2$: a) $0.23 \mu s$ after beginning of pulse; b) $0.36 \mu s$ after beginning of pulse; c) $1.6 \mu s$ after beginning of pulse (taken from reference 2).

TABLE 3.1
MAIN LINES OF CA AND CA+ RADIATING IN THE BAND $300 < \lambda < 650 \text{ nm}$

WAVELENGTH (nm)	E_u (cm^{-1})	g_u	A_{ul} (10^8 s^{-1})	$A_{ul}g_u$ (10^8 s^{-1})
Ca				
300.3	48551	9	1.08	9.7
363.7	42746	15	0.37	5.6
422.6	<u>23652</u>	3	2.18	6.5
430.0	38508	9	1.8	16.0
444.5	37754	15	0.85	12.7
559.2	38230	15	0.56	8.4
646.0	35820	21	0.54	11.34
Ca+				
317.3	56851	10	3.62	36.2
372.6	52167	2	2.49	5.0
{393.3}	<u>25414</u>	4	1.50	6.0
{396.8}	<u>25192</u>	2	1.46	2.9



A-7558

Figure 3.9. Degree of ionization in calcium plasma.

ions. We used a formula for the lowering based on the Debye length, λ_D , in the plasma⁷

$$\Delta E_j = \frac{(j+1)e^2}{\lambda_D} \quad (11)$$

where j is the charge of the atom/ion,

$$\lambda_D = kT \times \left\{ 4\pi(n_e + \sum z^2 [Ca^{z+}]) \right\}^{-1/2},$$

and e is the electron charge. One can readily derive from \bar{z} the electron density in a pure calcium plasma through the relation

$$n = 1.5 \times 10^{22} \rho \bar{z} \quad (12)$$

In the case of a gallstone or kidney stone, calcium represents only a fraction (f) per mass of the material. Since Ca and Ca^+ have lower ionization energies (6.1 and 11.9 eV) than the other atomic species (O, H, N, C), one expects that calcium will be ionized well before the others, so that, to a first approximation, we can still use Eq. (12) but must replace ρ by $f\rho$. For a calcium oxalate calculus, the fraction per weight of calcium is ~20%, leading to $f \approx 0.2$.

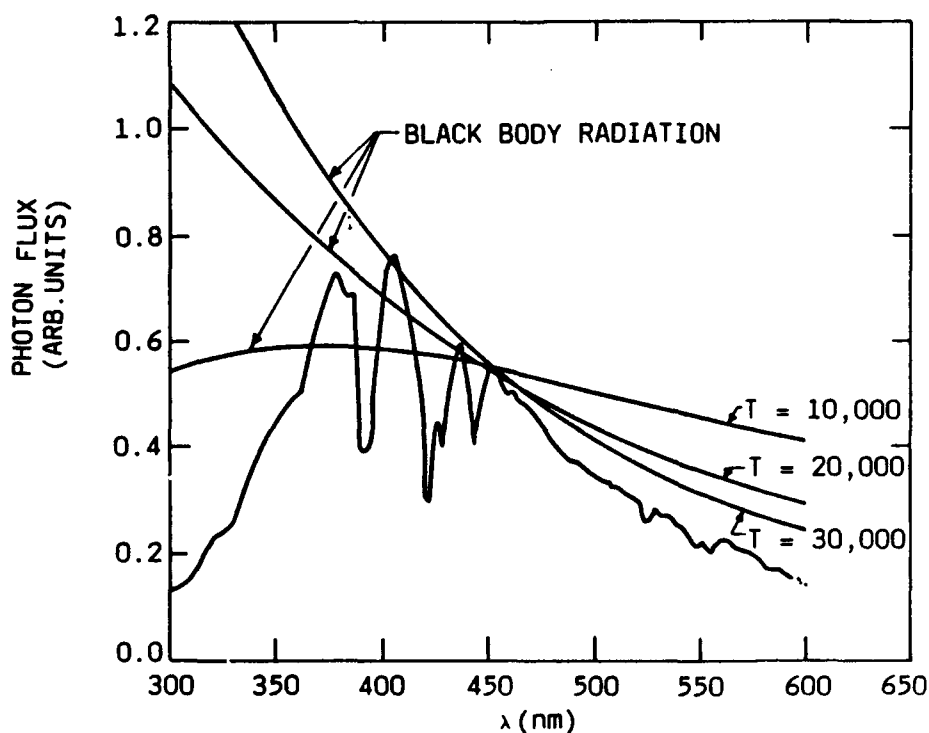
Analysis of Spectrum 3.8a

We estimate the electron density by looking at the Stark broadening of the two lines at 4450Å and 3920Å. The first line is a line of neutral calcium with full width half max of 70Å. From the line broadening parameters for the lines of Ca tabulated by Griem⁸, we estimate the electron density to be $4 \times 10^{18} \text{ cm}^{-3}$. At 3920Å we have two lines of Ca^+ separated by 35Å. Taking into account this separation, we estimate from the spectrum a full width half max for each line of 65Å corresponding to an electron density of $\sim 10^{20} \text{ cm}^{-3}$. These two densities are consistent with a plasma containing a hot core that radiates a continuum, surrounded by a cooler layer containing mainly Ca^+ and, further out, mainly Ca. The spectrometer in the experiments of Teng et al is looking at the plasma in a direction parallel to the surface. The cooler layer corresponds to plasma that has expanded laterally out of the laser beam. The electron density in the heated inner core is expected to be larger than 10^{20} cm^{-3} . We have attempted to derive the temperature of the inner core by

assuming that radiation in the continuum is black. We have plotted in Figure 3.10 several black body (BB) curves in units of photons / (cm²s nm) and normalized these curves so that they would pass through the point having ordinate 0.55 at $\lambda = 450$ nm. We have also plotted in Figure 3.10 the spectrum corresponding to Figure 3.8a. We see by comparing the spectrum to the BB curves that we cannot fit the continuum at $\lambda > 450$ nm with any BB curve. The continuum is inconsistent with a constant temperature black body. A possible explanation for the more rapid decrease in photon flux with increasing wavelength observed as compared to BB is the decreasing opacity of the plasma with decreasing wavelength. The absorption coefficient due to free-free and bound-free IB collisions varies with frequency as⁹

$$k \propto \frac{e^{h\nu/kT} - 1}{\nu^3}$$

The black body flux in the long wavelength limit varies proportionately with T for fixed ν . The spectrum indicates that the effective temperature seen by the radiometer decreases by a factor of at least two as λ increases from 450 to 600 nm.



A-7580

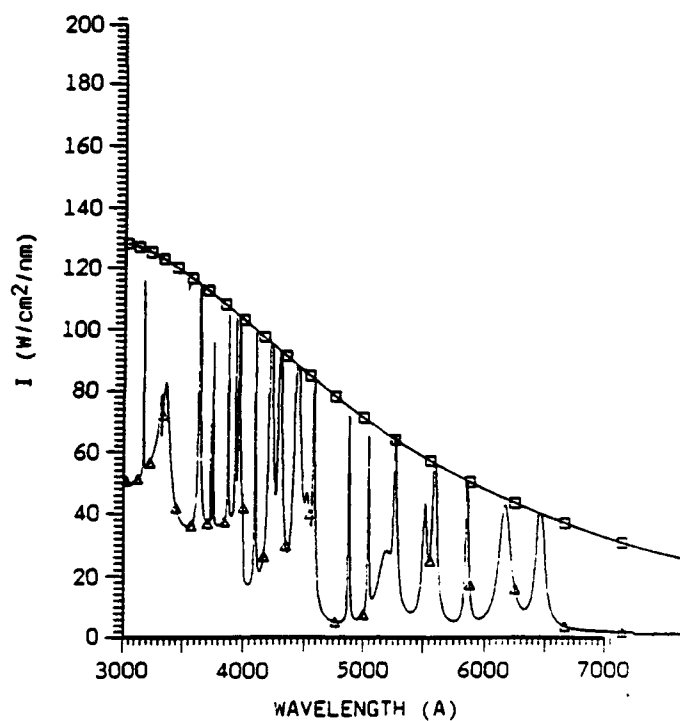
Figure 3.10. Comparison of blackbody spectral radiation curves with kidney stone plasma emission spectrum of Figure 3.8a.

The presence of calcium lines in absorption with electron densities in excess of 10^{20} cm^{-3} is consistent with a core density $> 10^{-2} \text{ g/cm}^3$ and a temperature $T > 15,000 \text{ K}$.

The spectrum in Figure 3.8b corresponds to a hotter but less dense plasma than in Figure 3.8a. The main lines of Ca^+ near 3920\AA appear in emission rather than in absorption. The feature at 320 nm is an emission line of Ca^+ . It is interesting to note that this line is absent from the earlier spectrum (Figure 3.8a). The spectrum (Figure 3.8c) corresponds to a much cooler vapor since the Ca^+ line at 316 nm has almost disappeared. The strongest line of Ca^+ at 393 and 396 nm are still apparent, indicating that Ca^+ has not completely recombined. The continuum is much weaker in the spectrum, indicating much lower electron densities than in the first two spectra. This is not surprising since after the pulse the plasma has expanded and the ions have recombined.

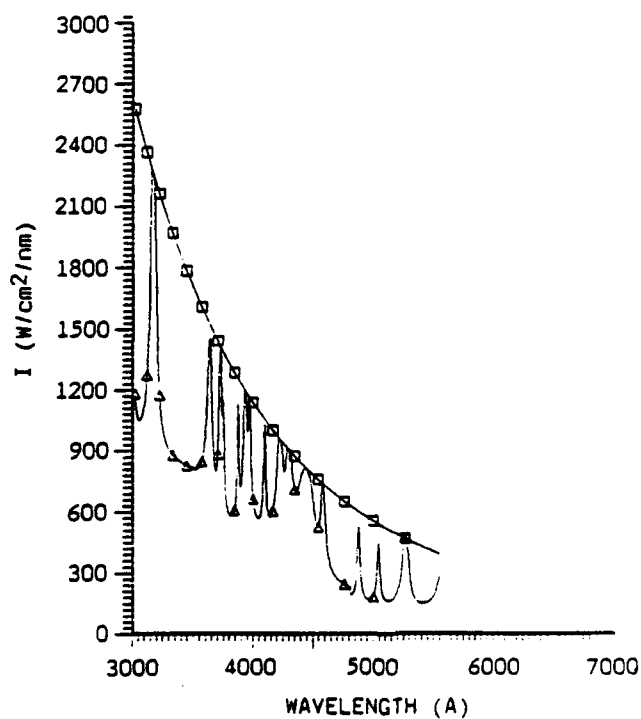
In order to better analyze the spectra, we have generated spectra of pure calcium plasmas using the PSI radiation code. This code calculates emission from isothermal slabs of a given thickness. The absorption coefficient of the plasma for free-free, bound-free, and bound-bound (line) transition is calculated and emission is calculated using Kirchhoff's law. The formulas used in the code are described in reference 10. The data on line strengths for Ca and Ca^+ was obtained from the NBS tabulations¹¹ and the Stark broadening parameters were taken from the book by Griem.⁸ We show below in Figures 3.11 to 3.16 plasma radiation in the $300\text{--}700 \text{ nm}$ band from slabs of thickness d . The fiber used in the experiments of Teng et al had a diameter of 0.34 mm . We allowed the thickness d to vary from 0.1 to 1 mm , which should pretty well cover the experimental conditions. Rather than use thermal equilibrium concentrations, we arbitrarily set the concentration of Ca , Ca^+ and Ca^{++} in order to better study the effect of dominant ions on plasma radiation.

Figure 3.11 shows radiation from a slab of thickness $d = 0.1 \text{ mm}$ at $T = 10,000 \text{ K}$ for a 10% ionized calcium plasma. We also show in this figure the black body envelope. The slab is seen to be optically thin except at line center. Figure 3.12 shows the spectrum emitted by a plasma of the same thickness as before but with $T = 25,000 \text{ K}$ and 50% ionized. The concentration



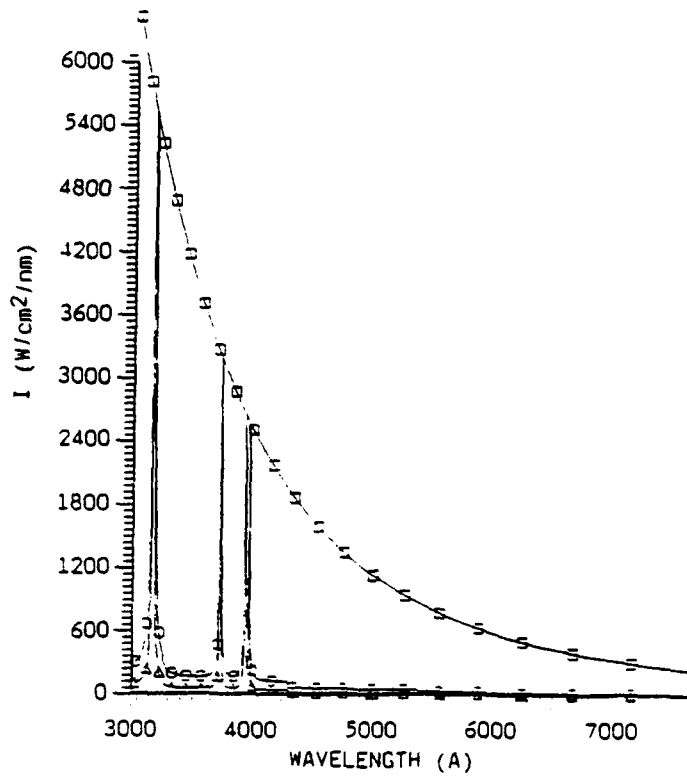
A-7579

Figure 3.11. Calcium slab emission for $T = 10,000$ K, $p = 5$ Atm, $n_e = [\text{Ca}^+] = 3.33 \times 10^{17} \text{ cm}^{-3}$ and $[\text{Ca}] = 3.3 \times 10^{18}$. Slab thickness = 0.01 cm.



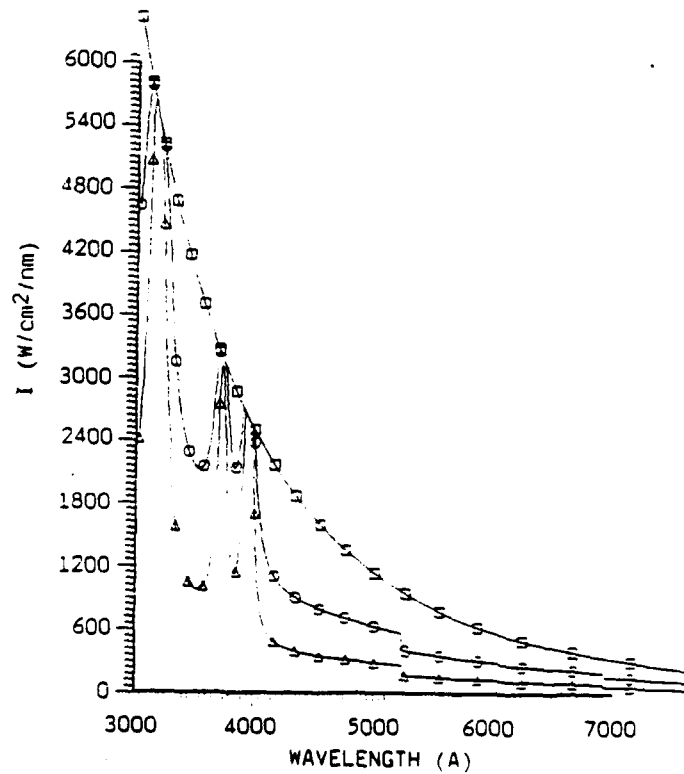
A-7578

Figure 3.12. Calcium slab emission for $T = 25,000$ K, $p = 34$ Atm, $n_e = [\text{Ca}^+] = [\text{Ca}] = 3.33 \times 10^{18} \text{ cm}^{-3}$. Slab thickness = 0.01 cm.



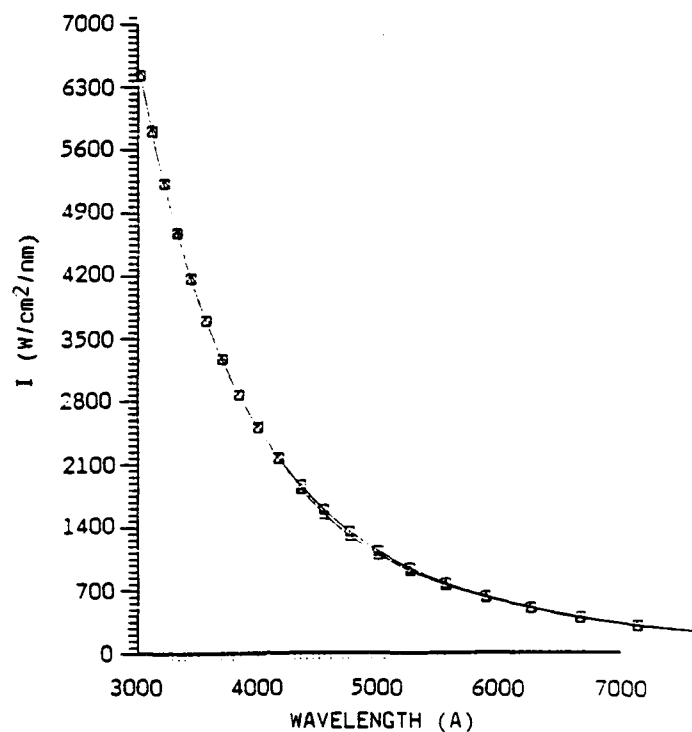
A-7577

Figure 3.13. Slab emission for $T = 40,000$ K, $\text{Ca}^+ = n_e = 10^{18} \text{ cm}^{-3}$, $p = 11$ Atm. $\Delta d = 0.01$ cm, $\square d = 0.03$ cm.



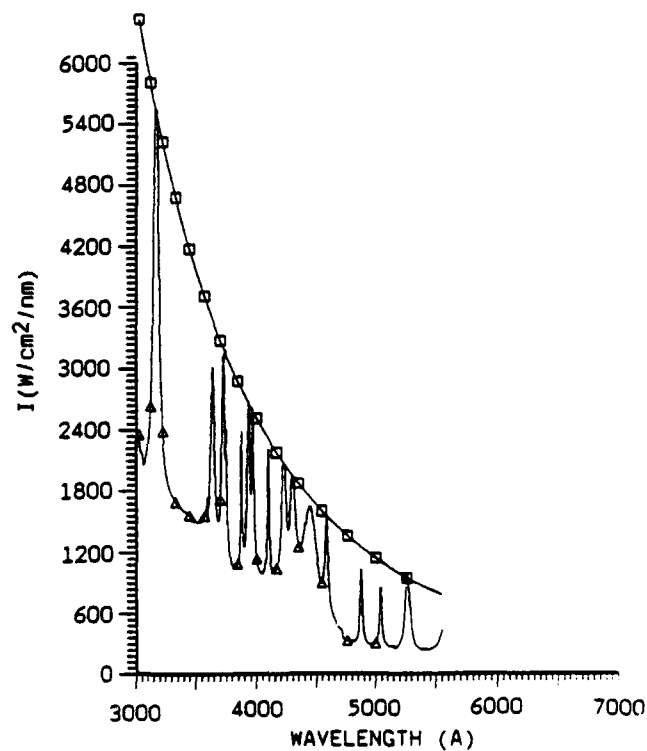
A-7576

Figure 3.14. Slab emission for $T = 40,000$ K, $[\text{Ca}^+] = n_e = 10^{19} \text{ cm}^{-3}$, $p = 110$ Atm. $\Delta d = 0.01$ cm, $\square d = 0.03$ cm.



A-7575

Figure 3.15. Slab emission for $T = 40,000$ K, $[Ca^+] = [n_e] = 10^{20} \text{ cm}^{-3}$, $p = 1100 \text{ atm}$. $\Delta d = 0.01 \text{ cm}$, $\square d = 0.03 \text{ cm}$.



A-7574

Figure 3.16. Slab emission for $T = 40,000$ K, $n_e = [Ca^+] = [Ca] = 3.33 \times 10^{18} \text{ cm}^{-3}$, $d = 0.01 \text{ cm}$.

of Ca is the same in both spectra. The tenfold increase in electron density caused the lines to broaden significantly. Figures 3.13 to 3.16 correspond to a fully singly ionized calcium plasma at 40,000 K and shows the effect of density on plasma radiation. The Ca^+ density is allowed to vary from 10^{17} cm^{-3} ($\rho = 6.7 \times 10^{-5} \text{ g/cm}^3$) to 10^{20} cm^{-3} ($\rho = 6.7 \times 10^{-3} \text{ g/cm}^3$). The slab is seen to be completely black at the highest density considered. Introduction of an equal amount of non-ionized calcium shown in Figure 3.16 is seen to add significant structure to the spectra.

We show in Figure 3.17 the photon flux emitted by a plasma slab of density 10^{-3} g/cm^3 and temperature 15,000 K. The composition chosen was that corresponding to thermodynamic equilibrium. The spectra of this figure can be directly compared with the measured spectra since the detector response in Teng et al's experiments was proportional to photon flux. We note that the Ca^+ line at 320 nm is black and radiates more than the fundamental line at

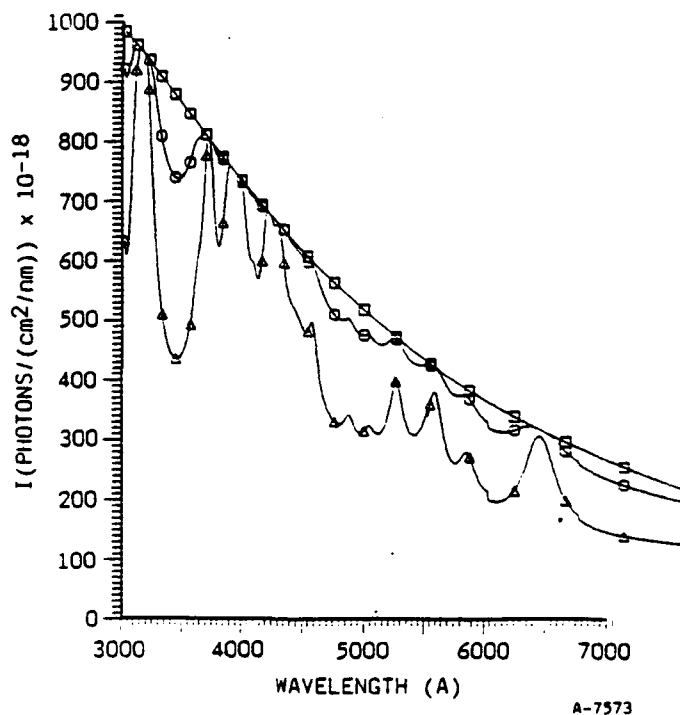


Figure 3.17. Photon flux emitted by a slab of thickness d in thermal equilibrium, $T = 15,000 \text{ K}$, $p = 60 \text{ Atm}$, $\rho = 10^{-3} \text{ g/cm}^3$.
 $n_e = 1.41 \times 10^{19}$, $[\text{Ca}] = 1.37 \times 10^{17}$, $[\text{Ca}^+] = 1.33 \times 10^{19}$,
 $[\text{Ca}^{++}] = 4.2 \times 10^{17} \text{ cm}^3$.

400 nm due to the effect of the black body envelope. The spectra in Figure 3.8b, however, indicates a weaker line at 320 nm than at 400 nm. The only way to reconcile the two spectra (outside of assuming that the spectrum of 3.8b corresponds to a much lower temperature, where Ca⁺ should normally be absent) is to assume that the spectral response is falling off at short wavelengths (due to glass optics). Teng et al, however, report using quartz windows and optical elements.

REFERENCES

1. Watson, G., Laser Lithotripsy (Unpublished thesis).
2. Teng, P., Nishioka, N., Anderson, R. and Deutsch, T. "Optical studies of pulsed laser fragmentation of biliary calculi," Appl. Phys., B, pp. 42-73 (1987).
3. Glass, A.J. and Guenther, A.H., Proceedings of the Annual Conference on Laser Damage (American Society for Testing Materials, Philadelphia, 1969), Spec. Publ. 469; Natl. Bur. Stand. (U.S.) Spec. Publ. 341 (1970); 372 (1972); 387 (1973), 414 (1974), 435 (1975), 462 (1976), 509 (1977), 541 (1978), 568 (1979), 688 (1985).
4. Bloembergen, N., "Laser induced electric breakdown in solids," IEEE J. Quantum Electron., QE-10, pp. 375-386 (1974).
5. Sparks, M. and Duthler, M.J., "Theory of infrared absorption and material failure in crystals containing inclusions," J. Appl. Phys., 44, pp. 3038-3045 (1973).
6. Anisomov, S.I. and Makshantsev, B.I., "Role of absorbing inhomogeneities in the optical breakdown process," Sov. Phys. Solid State, pp. 743-745 (1973).
7. Griem, H., Plasma Spectroscopy (McGraw Hill, New York, 1964), p. 139.
8. Ibid., Table 4-5.
9. Zel'dovich, Ya B. and Raizer, Yu. P., Physics of Shock Waves and High-Temperature Hydrodynamic Phenomena (Academic Press, New York, 1966), p. 271.
10. Pirri, A., Root, R. and Wu, P. "Analytical Laser/Material Interaction Investigations," PSI TR-104, Physical Sciences, Inc., Woburn, MA 01801, September 1977.
11. Atomic Transition Probabilities: Neon Through Calcium. Vol. II., National Bureau of Standards special publication NBS-22. Government Printing Office, Washington, DC 20402 (1969).

4. MECHANICAL FRAGMENTATION MODELING

Mechanical fragmentation of kidney stones under laser irradiation appears to be associated with the vaporization of a portion of the calculus and the subsequent ionization and plasma formation. This high pressure plasma is believed to generate a fragmentation shock wave which propagates into the stone. Below, a mathematical model is developed to describe this phenomena and is used to suggest the optimum laser waveform that will yield the minimum energy requirements (minimum energy per gram removed).

Initially, laser pulse energy E_p is deposited in length over area A to obtain energy density e

$$e = \frac{E_p}{A}$$

where is the effective optical absorption depth, λ , plus the thermal diffusion depth over the pulse duration τ_p ,

$$= \lambda + \sqrt{K\tau_p}$$

where K is the thermal diffusivity. When energy density e exceeds the vaporization threshold, plasma formation is imminent. We write

$$e > \rho_\infty H_v$$

where H_v is the vaporization energy per gram and ρ_∞ is the local bulk density of the porous stone ($\rho_\infty \sim 1.5$ g/cc). The mass m vaporized by the pulse is simply $m = E_p/H_v$.

From the data of Watson (THESIS) determining the fluence ($F_p = E_p/A$) associated with the fragmentation threshold, we deduce

$$\lambda \sim 10-20 \text{ } \mu\text{m} ,$$

$$H_v \sim 10 \text{ kJ/g} ,$$

and

$$K = 0.03 - 0.1 \text{ cm}^2/\text{s}$$

where the value of K is consistent with that of $0.06 \text{ cm}^2/\text{s}$ for limestone and $0.02 \text{ cm}^2/\text{s}$ for CaO . The threshold fluence associated with vaporization and fragmentation becomes

$$F_{th} = \rho_{\infty} H_v (\lambda + \sqrt{K\tau_p})$$

where we will arbitrarily employ

$$\begin{aligned} F_p < 1/3F_{th} & : \text{No Fragmentation} \\ 1/3F_{th} < F_p < F_{th} & : \text{Onset Region} \\ F_p > F_{th} & : \text{Fragmentation} \end{aligned}$$

The actual pressure history and impulse delivered to the stone are complicated functions of plasma formation, bubble formation and bubble collapse. While Sections 3 and 5 attempt to deal with these issues in some detail, a crude model must be generated here in order to assess the shock fragmentation phenomenology.

If the stone were irradiated in air, the vapor would leave the stone with the velocity (V) of sound in a gas with the molecular weight of CaO at approximately 1000°C .

$$V \sim 4 \times 10^4 \text{ cm/s}.$$

The momentum I_a imparted to the stone is mV , and the coupling coefficient C_{I_a} becomes

$$C_{I_a} = \frac{I_a}{E_p} = \frac{V}{H_v} \sim 4 \frac{\text{dyne}\cdot\text{sec}}{\text{Joule}}$$

and is known as the "transparent vapor limit" because there is no beam absorption above the surface by either the air or the vapor. Calculations appropriate to the limit of complete air/vapor absorption (Simons, 1984)

suggest 6.9 dyne.sec/Joule. In the absence of any evidence of plasma formation in air, the pressure on the stone in air (p_a) is determined in the transparent vapor limit

$$p_a = \frac{C_{I_a} F_p}{\tau_p} .$$

Noting that a 1.5 μ s, 30 J/cm² pulse satisfies the threshold criterion (F_{th}) above, the pressure on the stone becomes

$$p_a = 80 \text{ bar} .$$

When the stone is irradiated under water, much larger pressures and impulses are transferred to the stone. Teng et al have observed that the pressures under water may be as much as 12 times greater than in air. If the corresponding impulse coupling coefficient is increased by 12, we obtain

$$C_{I_w} \sim \frac{50 \text{ dyne.sec}}{\text{Joule}} .$$

Until a more rigorous model of bubble growth and collapse (Section 5) is developed, the pressure imparted to a stone submerged in water is assumed to be constant during the pulse and given by an impulse coupling coefficient of 50 dyne.sec/Joule.

$$p = C_{I_w} F_p / \tau_p$$

A one-dimensional slug model is used to describe the interaction of a high-intensity laser pulse with a porous kidney stone. The mass loss due to vaporization is neglected and the interaction is approximated by replacing the laser pulse by a one-dimensional piston pushing on the target surface with the equivalent pressure. When the pressure is greater than the strength of the porous stone, $\bar{\sigma}_u$, a fracturing shock wave will propagate into the target. The zone between the shock front and the piston is filled with the fragmented target debris. The analytic model (Simons and Legner, 1982) for the Shock Hugoniot in a porous material is used to obtain the conditions behind the shock. The density ρ of the partially compressed fragmented porous material behind the shock is given by

$$\frac{\rho}{\rho_0} = \frac{\left(1 + \frac{\Gamma}{2}\right) p K_0 + 1}{1 + \frac{\Gamma p K_0}{2(1-\theta)}}$$

where p is the pressure induced by the laser pulse, K_0 is the cold compression coefficient of the kidney stone, Γ is the Grüneisen coefficient, θ is the porosity, and ρ_0 is the non-porous density of the stone. The fracture shock velocity, V_f , can then be written as

$$V_f = \left[\frac{\rho p}{\rho_\infty (\rho - \rho_\infty)} \right]^{1/2}$$

where ρ_∞ is the bulk density of the porous material in front of the shock.

$$\rho_\infty = \rho_0 (1-\theta) .$$

Since the physical properties of kidney stones are not readily available, the properties of CaO will be used whenever possible. Hence, we use

$$\rho_0 \sim 3\text{g/cc}$$

$$\theta \sim 0.5$$

$$\rho_\infty \sim 1.5\text{g/cc}$$

$$\Gamma \sim 2^*$$

$$K_0 \sim 3.5 \times 10^{-12} \text{ cm}^2/\text{dyne}$$

and,

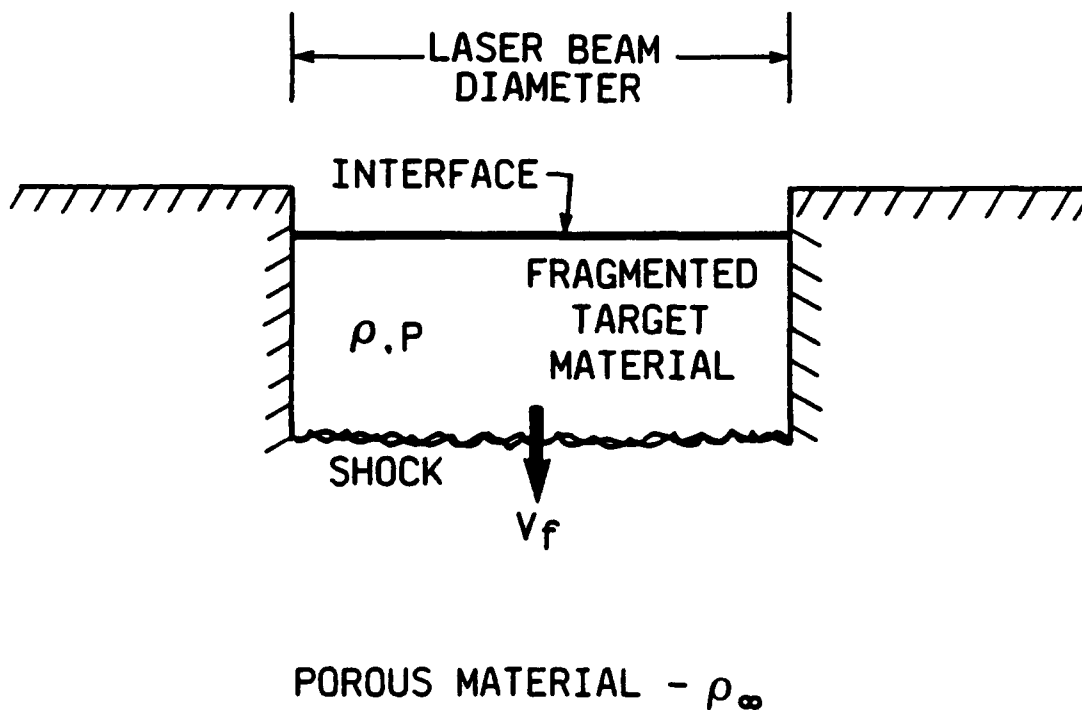
$$\bar{\sigma}_u = 80 \text{ bar} .$$

where the choice of 80 bar for $\bar{\sigma}_u$ is non-trivial. Handbook values for the compressive strength of concrete and limestone are upwards of 350 bar with corresponding values of the limiting shear at 80 bar. Since kidney stones are approximately 50% porous, we consider their ultimate strengths to be 175 bar in compression and 40 bar in shear. When a material is subjected to a one-dimensional compression of strength $\bar{\sigma}$, the corresponding shear 45° off axis is $\bar{\sigma}/2$. Hence, when $\bar{\sigma}$ is 80 bar, the material will fail in shear at 45°

* varies between 1.5 and 2.5 for metals and reduces to $\gamma-1$ for a gas. We assume a value of 2 for Γ .

to the principal load and not in compression on the principal axis. This value of $\bar{\sigma}_u$ is supported by compressive tests we have performed on stones in our laboratory, indicating failure in the range of 60 bar to 110 bar.

At the end of the laser pulse, a high pressure slug of fragmented target material of density ρ is lodged in the stone as illustrated in Figure 4.1. Following the deposition of energy by the laser, the pressure constraint (i.e., the piston) at the interface is removed and a rarefaction wave begins to propagate toward the shock front. The shock wave continues to propagate into the target until the rarefaction wave reaches the shock front and reduces its pressure to $\bar{\sigma}_u$.



A-7145

Figure 4.1. Stone fragmentation at the end of the laser pulse.

For the description of the flowfield after the laser pulse is off, a simplified Arbitrary Lagrangian-Eulerian computer program (Amsden et al., 1980), SALE, is used. The hydrodynamic code-SALE was originally developed at the Los Alamos Scientific Laboratory and is available at the National Energy Software Center, Argonne National Laboratory, Argonne, Illinois. The SALE code combines an implicit treatment of the pressure equation similar to that in the Implicit Continuous-Fluid Eulerian (ICE) technique with the grid rezoning philosophy of the Arbitrary Lagrangian-Eulerian method. As a result, it can handle flow speeds from supersonic to the incompressible subsonic limit in a grid that may be moved with the fluid in typical Lagrangian fashion, held fixed in a Eulerian manner, or moved in some arbitrary way to give a continuous rezoning capability.

The SALE code offers flexibility in specifying the equation of state of the shock layer. For the present calculations, an ideal gas assumption is made for the fragmented target material. In general, the "SESAME TABLE," which is the tabulated equation of state for numerous materials compiled by the Los Alamos National Laboratory, may be used.

Illustrative examples of the results of the SALE code have been obtained for the sample case of a 1 μ s pulse with a fluence of 200 J/cm², irradiated onto a 50 percent porous kidney stone. The density, pressure, and velocity contours corresponding to a time 0.64 μ s after the pulse are illustrated in Figures 4.2 through 4.4, respectively. The contours clearly demonstrate that the fragmented target debris has expanded well outside the crater. This expansion enhances the dissipation of the impact energy through the debris velocity.

The goal of the present calculations is to assess the effects of the pulse fluence and pulse time on the fracturing of kidney stones by laser radiation. Figure 4.5 illustrates the crater depth as a function of pulse time for various pulse fluences. For a pulse fluence of 200 J/cm², the crater depth increases from about 4×10^{-2} cm at $\tau_p = 10^{-7}$ s to approximately 1.5 cm at $\tau_p = 10^{-4}$ s. Since the pulse fluence and the coupling coefficient are assumed to be constant, the pressure decreases with increasing pulse duration (decreasing laser intensity). In the one-dimensional limit, there is no

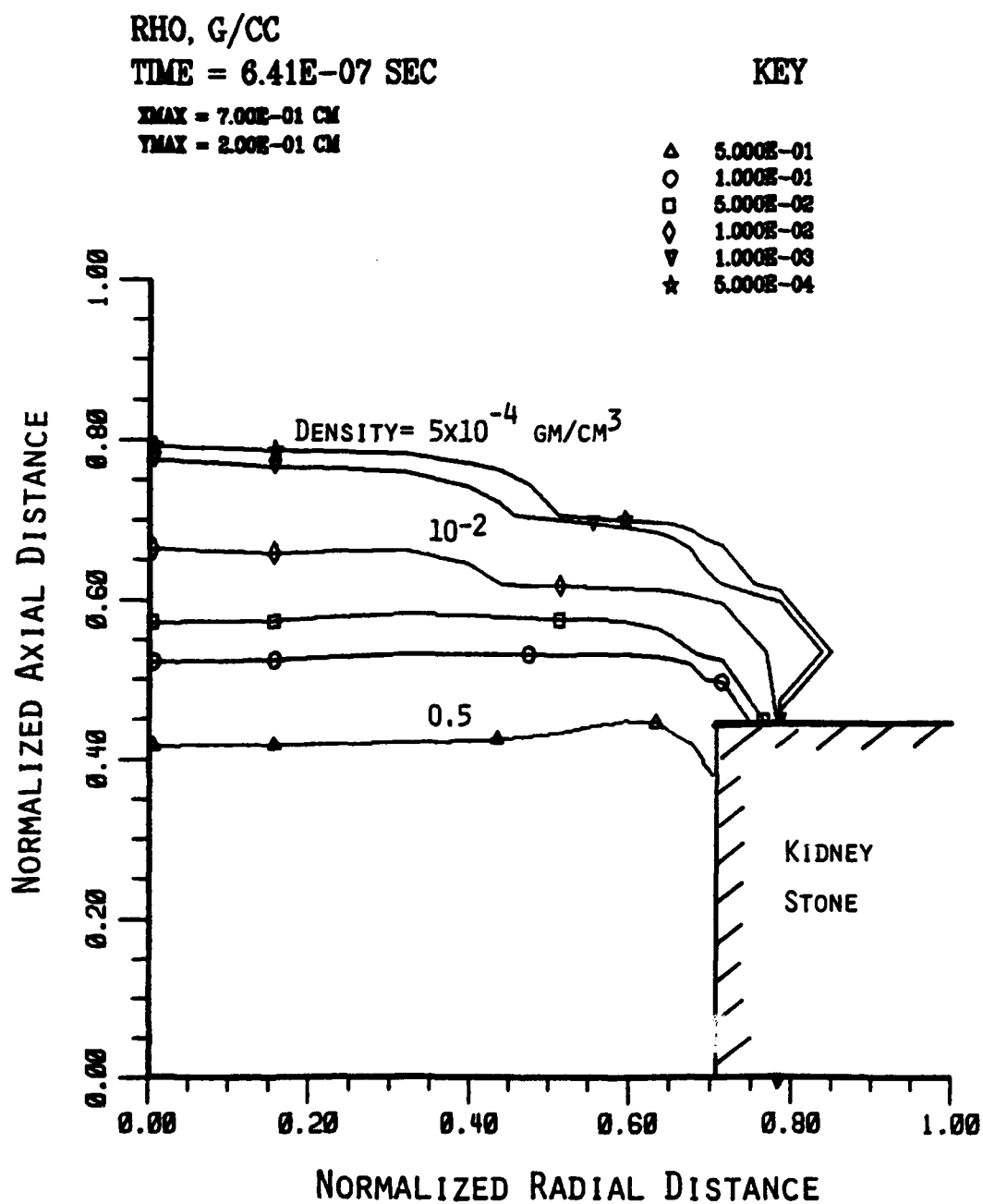


Figure 4.2. Density contours at 1 μ s after laser energy deposition.

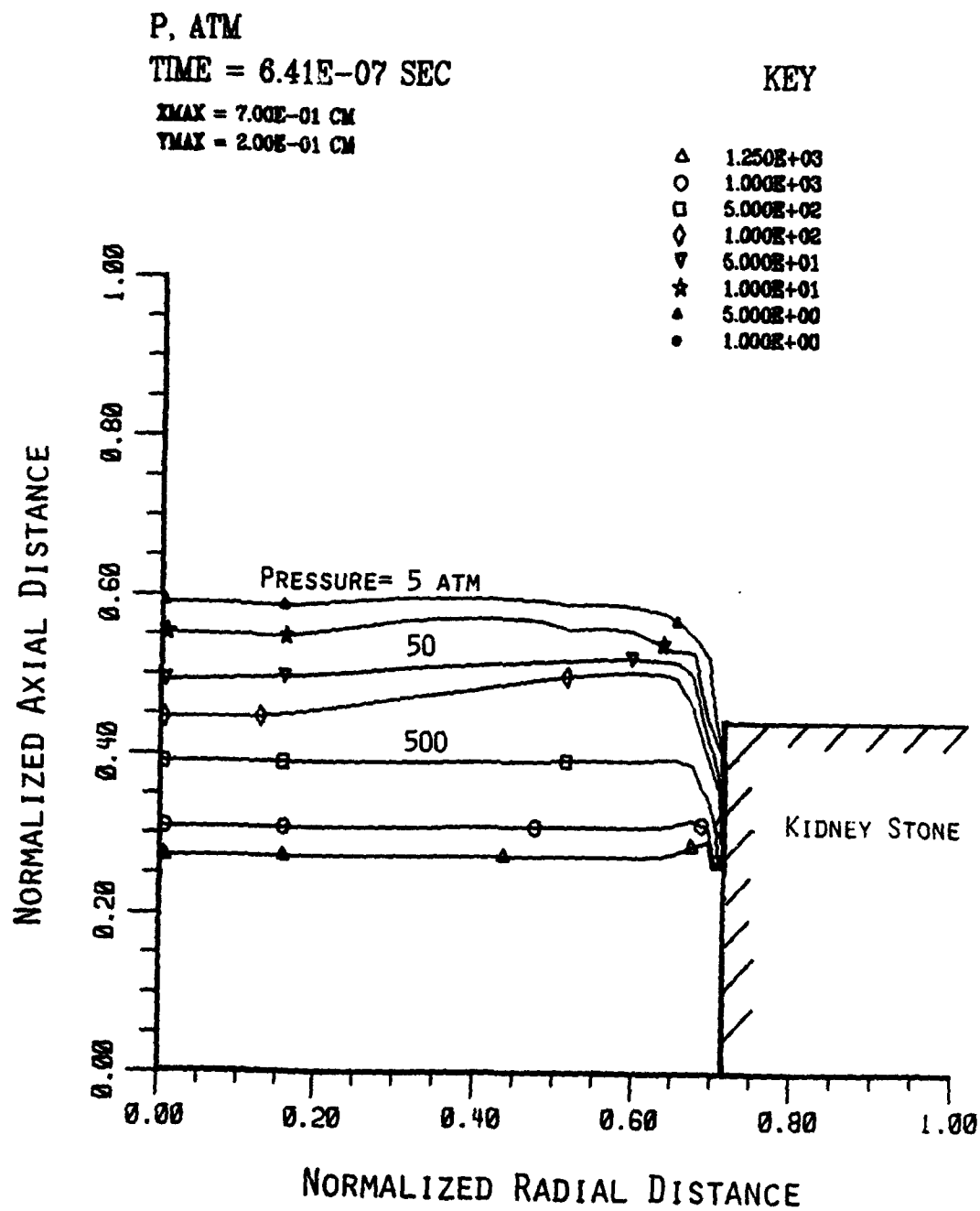


Figure 4.3. Pressure contours at 1 μ s after laser energy deposition.

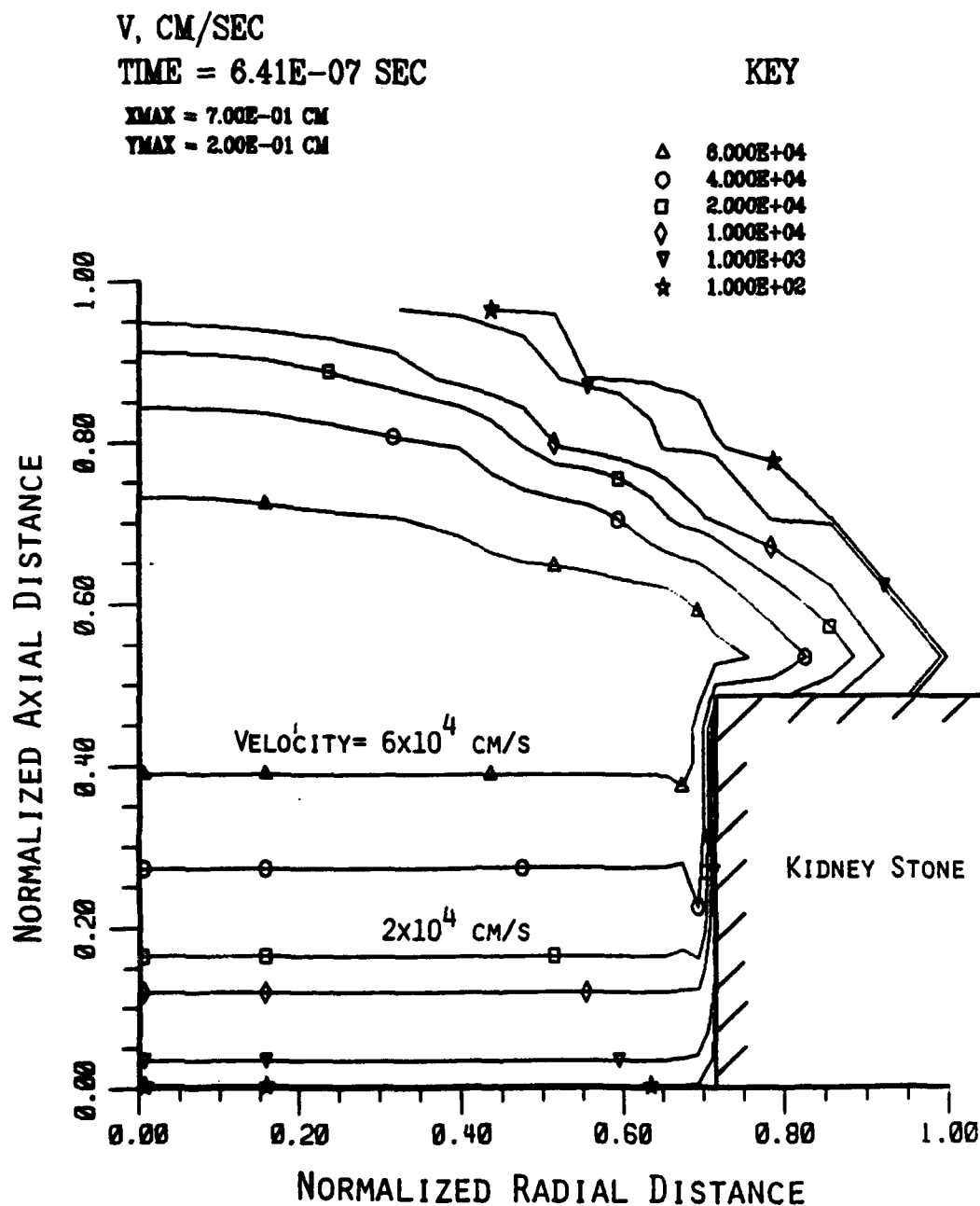
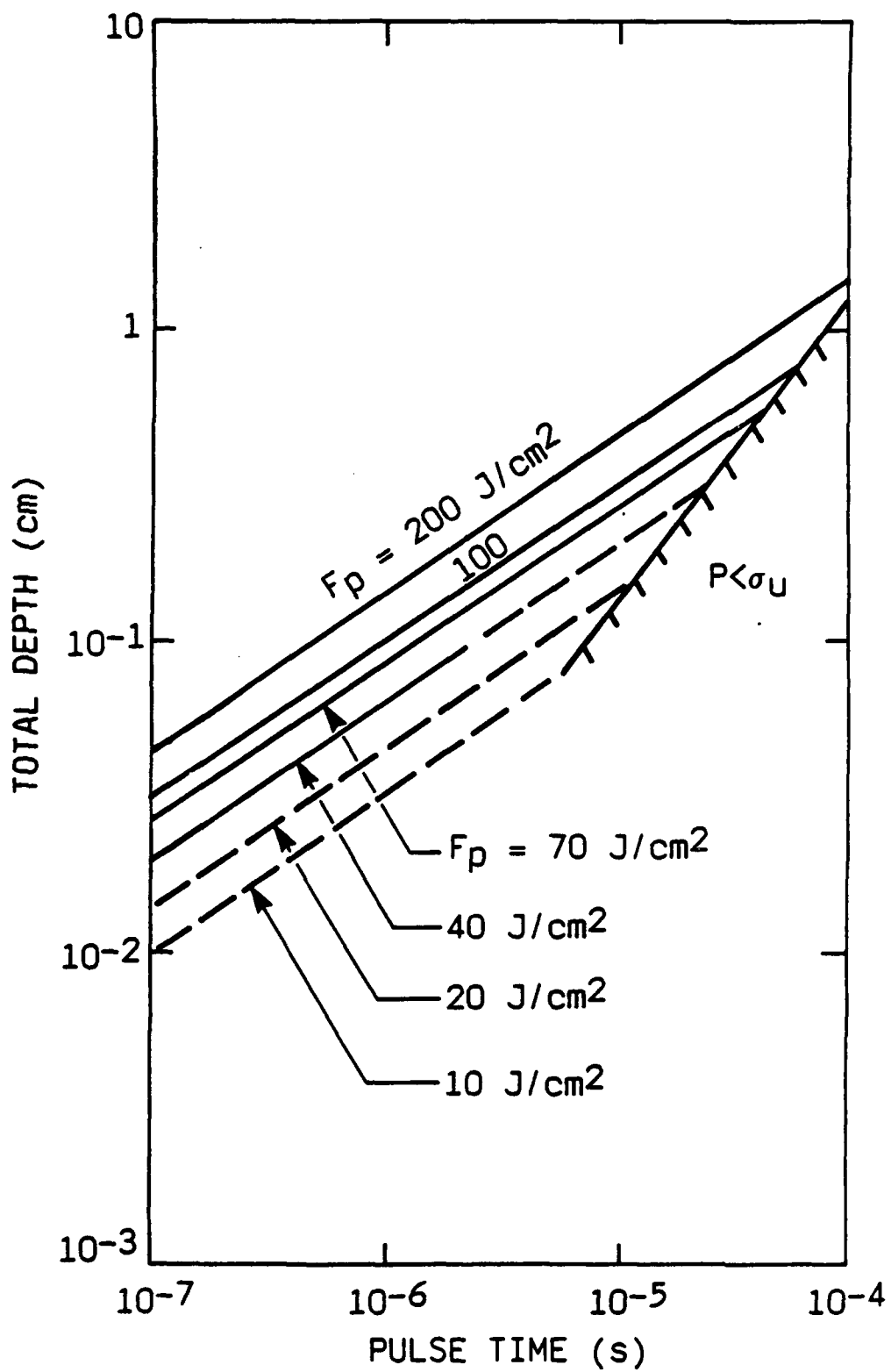


Figure 4.4. Axial velocity contours at 1 μ s after laser energy deposition.



A-7945

Figure 4.5. One-dimensional crater depth.

geometric decay of the fragmentation shock and lower pressures applied over longer times yield deeper craters. The deepest crater then occurs when the induced pressure just exceeds the strength of the stone. However, the three-dimensional decay of the pressure pulse will seriously alter this result. We presently plan to treat three-dimensional effects in the coming year.

The present calculations also demonstrate the obvious result that the crater depth decreases with decreasing pulse fluence until that fluence is below the fragmentation threshold. The dashed lines represent calculations in the "onset region"

$$\frac{1}{3} F_{th} < F_p < F_{th} .$$

The energy required for the mass removal is defined as E_η

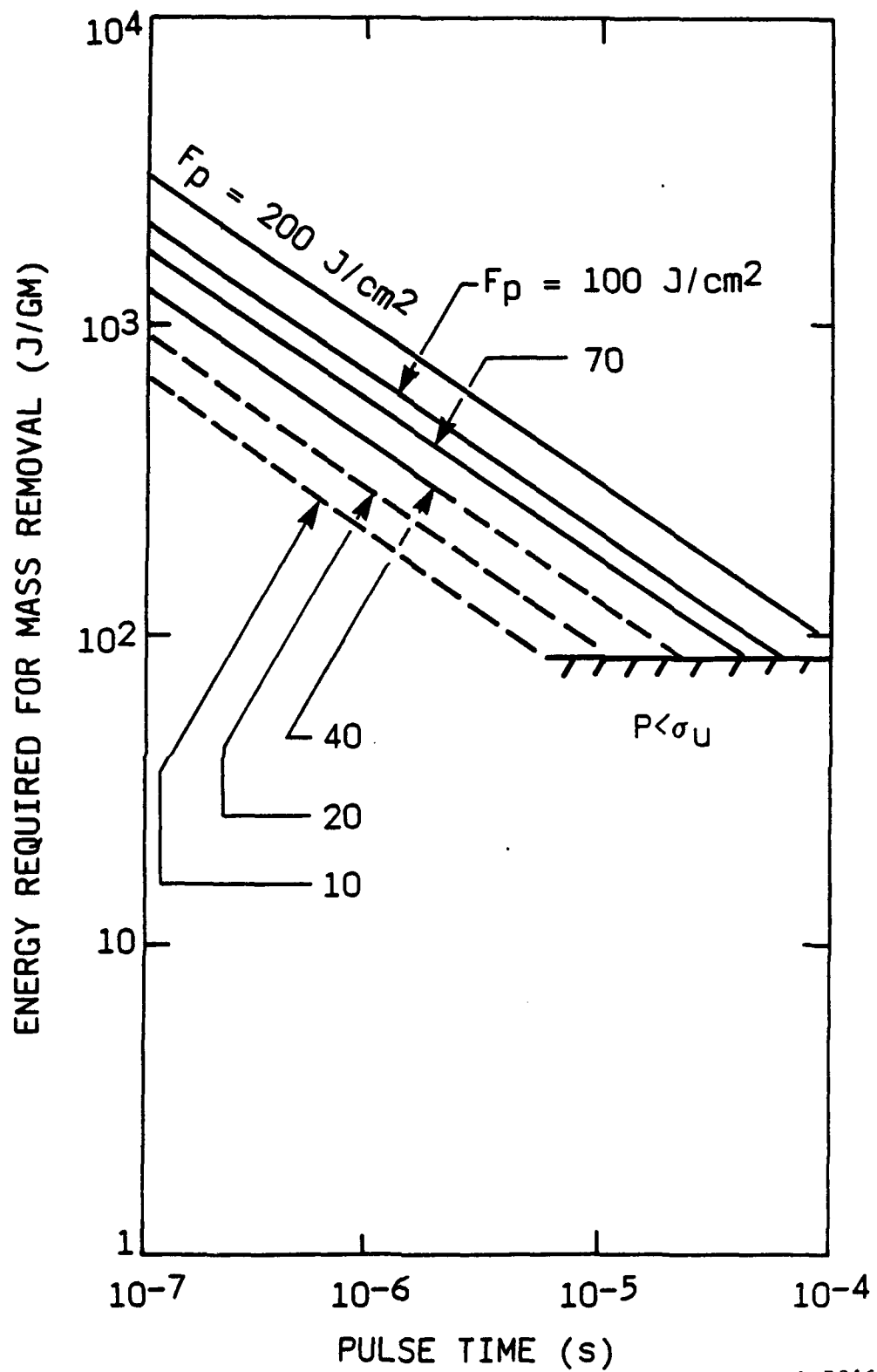
$$E_\eta = \frac{F_p}{\rho \times \text{Depth}}$$

and is shown in Figure 4.6. For a pulse fluence of 200 J/cm^2 , the energy required to remove a unit mass of stone decreases from $3 \times 10^3 \text{ J/gm}$ at 10^{-7} s to about 10^2 J/gm at 10^{-4} s . The minimum energy requirement occurs at the point where the pressure provided by the laser pulse is just above threshold. This is largely due to the one-dimensional approximation. The energy efficiency also increases (energy decreases) with decreasing pulse fluence until below threshold. Again, the dashed lines represent the pulse fluence in the range

$$\frac{1}{3} F_{th} < F_p < F_{th} .$$

The above calculations suggest a maximum energy efficiency (minimum energy/mass) when operating just above the threshold of mechanical fragmentation. These predictions are, however, subject to many approximations:

- 1) one-dimensional geometry
- 2) constant pressure over the pulse duration
- 3) $50 \text{ dyne} \cdot \text{sec/Joule}$ coupling coefficient
- 4) porous Shock Hugoniot for porous volumes that are filled with air.
- 5) the neglect of spall phenomena



A-7946

Figure 4.6. Mass Removal Efficiency.

5. A SIMPLIFIED MODEL FOR LASER LITHOTRIPSY

- Modeling of the Above-Surface Fluid Dynamics -

Laser lithotripsy appears to depend upon laser-induced breakdown at or near the surface of a high pressure bubble. The resulting breakup of the stone depends upon the resulting spatial and temporal pressure history which the stone is subjected to. The purpose of this analysis is to suggest a simplified method for treating the fluid mechanics of the problem. Hopefully, this would be helpful both in optimizing laser pulse characteristics and in using acoustic signals to assist in assessing effectiveness.

The overall flow problem may be separated into treatment of the vapor bubble on the one hand and treatment of the resulting flow in the essentially incompressible fluid surrounding it on the other. Since, in general, the fluid, which we will assume to have the properties of water, represents significant inertia, its flow over a wide range of conditions can be approximated quite well by a linearized or acoustic model. Thus, we will assume that the water flow is described by sound waves spreading outward from the vapor bubble.

The boundary condition at the surface of the bubble is that the pressure and expansion velocity of the bubble must match the pressure and fluid velocity of the water.

The vapor bubble, on the other hand, will tend to expand slowly compared to the sound speed in the vapor. Thus, the vapor bubble may be treated as a uniform pressure region. The properties of the vapor will be determined by absorption of laser energy and by loss of energy by reradiation and by PV work done on the surrounding water.

The assumptions introduced thus far are valid if the expansion velocity of the bubble is small compared to the sound speed in both the water and the vapor bubble. Actually, the results may be somewhat forgiving as to violation of the first condition since the radial expansion of the wave in the water will rapidly reduce the strength of the wave.

Vapor Bubble

For the present analysis, we will further assume that the temperature and density within the vapor bubble are uniform and that the heat capacity can be represented by a constant. The latter assumption neglects heats of ionization, dissociation, and vaporization.

The energy equation is then given by

$$\frac{d(\rho C_v T V)}{dt} + p \frac{dV}{dt} = \frac{dE}{dt} \quad (1)$$

or

$$\frac{\gamma}{\gamma-1} p \frac{dV}{dt} + \frac{1}{\gamma-1} V \frac{dp}{dt} = \frac{dE}{dt} \quad (2)$$

where ρ is the density, C_v is the heat capacity at constant volume, T is the temperature, V is the total volume of the gas bubble, p is the pressure, dE/dt is the rate of absorption of laser energy (or minus the rate of reradiation), and γ is the ratio of specific heats.

For the case of $dE/dt = 0$, this reduces as expected to

$$pV^\gamma = \text{constant} = p_0 V_0^\gamma \quad (3)$$

Note that within the approximation of negligible heat of vaporization this is true independent of the amount of vaporization which has occurred.

One-Dimensional Planar Geometry

For illustrative purposes, let us first consider the planar one-dimensional case. In this case, V and E are to be interpreted as the volume and net energy absorbed per unit area respectively. Thus, V becomes simply the linear thickness of the vapor bubble and the velocity at the edge of the bubble is given by

$$u = dV/dt \quad (4)$$

For waves moving outward only (towards positive x), the pressure and velocity in the water are functions of $[ct - x]$ only and not of $[ct + x]$, where c, t, and x are the speed of sound in the water, the time, and the position respectively. Further, the acoustic equations give

$$\delta p = \rho_l c \delta u \quad (5)$$

as the change across each elemental wave (where ρ_l is now the density of the liquid). Taking the initial uniform pressure as p_∞ and the initial velocity as zero throughout the medium, we may integrate (5) to

$$p = \rho_l c u + p_\infty \quad (6)$$

Within the acoustic approximation, the vapor-fluid boundary is essentially at $x = 0$. Using equations 2, 4, and 6 and matching velocity and pressure at the boundary, we obtain

$$\frac{\gamma}{\gamma-1} \left(p_\infty + \rho_l c \frac{dV}{dt} \right) \frac{dV}{dt} + \frac{\rho_l c V}{\gamma-1} \frac{d^2 V}{dt^2} = \frac{dE}{dt} \quad (7)$$

for the vapor volume. Since the above relations relate V and its derivatives to pressure and velocity, and since these are constant along lines of constant $ct-x$, integrating Eq. (7) for a given dE/dt defines the entire flow field. Thus, provided that a reasonable approximation to dE/dt exists, numerical integration of Eq. (7) will provide a solution.

For the present, let us consider only the highly simplified case of a very short laser pulse and examine the flow field only in the period after the end of light absorption, $dE/dt = 0$. In this case, we may use equations 3, 4, and 6 to obtain

$$\left(p_\infty + \rho_l c \frac{dV}{dt} \right) V^\gamma = p_0 V_0^\gamma \quad (8)$$

or

$$\rho_l c \frac{dV}{dt} = p_0 \left(\frac{V_0}{V} \right)^\gamma - p_\infty \quad (9)$$

Thus, when the pressure is initially large compared to p_∞ , the volume will grow as $t^{1/\gamma+1}$ and the pressure will decay as $t^{-\gamma/\gamma+1}$. At late times, the volume will asymptotically approach $V_0(p_0/p_\infty)^{1/\gamma}$, corresponding to the pressure asymptotically approaching the ambient pressure p_∞ .

Experimental observations of roughly spherical bubble formation indicate that the bubble reaches a maximum size and then collapses. In the present planar case, the theory does not predict the collapse. The difference is presumably due to the difference in the number of dimensions.

Spherically Symmetric

In the spherically symmetric case, the acoustic solution for outgoing waves only is given by

$$r\phi = f[ct-r] \quad (10)$$

where f is an arbitrary function of $[ct-r]$, r is the radial coordinate,

$$p = \rho \ell \frac{\partial \phi}{\partial t} + \text{const} = \rho \ell c \frac{f'}{r} + p_\infty \quad (11)$$

and

$$u = - \frac{\partial \phi}{\partial r} = - \frac{\partial \left(\frac{f}{r} \right)}{\partial r} = - \frac{f'}{r} + \frac{f}{r^2} . \quad (12)$$

At the edge of the bubble, $r = a$, we may assume that $f'/a \ll f/a^2$ since f will vary on a scale of ct , which under the acoustic assumption is large compared to a . Thus, the velocity at the edge of the bubble, U_e , can be approximated as

$$U_e = \frac{da}{dt} = \frac{f}{a^2} \quad (13)$$

Since

$$V = \frac{4\pi}{3} a^3 , \quad (14)$$

Eq. (13) becomes

$$f = \frac{1}{4\pi} \frac{dV}{dt} \quad (15)$$

and using Eq. (11), Eq. (2) becomes

$$\frac{1}{\gamma-1} \left(\frac{(\gamma-1/3)\rho\ell}{(48\pi^2)^{1/3}} V^{-1/3} \frac{d^2V}{dt^2} + \gamma p_\infty \right) \frac{dV}{dt} + \frac{\rho\ell}{(\gamma-1)(48\pi^2)^{1/3}} V^{2/3} \frac{d^3V}{dt^3} = \frac{dE}{dt} \quad (16)$$

which again can be integrated numerically for a given dE/dt to define the entire flow and pressure field.

If we look again at the simplified case of a very short laser pulse so that in the solution region $dE/dt = 0$, Eq. (3) becomes

$$\frac{\rho\ell}{(48\pi^2)^{2/3}} \frac{d^2V}{dt^2} = \left(p_0 \left(\frac{V_0}{V} \right)^\gamma - p_\infty \right) V^{1/3} \quad (17)$$

Multiplying both sides by dV/dt and integrating, one obtains

$$\rho\ell \left(\frac{dV}{dt} \right)^2 = \frac{3}{2(48\pi^2)^{1/3}} \left(\frac{p_0 \left(\frac{V_0}{V} \right)^\gamma}{1 - \frac{3\gamma}{4}} - p_\infty \right) V^{4/3} + A \quad (18)$$

The integration constant, A , would be determined by the initial conditions, i.e., integration of Eq. (16) during the laser pulse. Thus far, we have been unable to find a satisfactory approximation, short of this integration, for determining A .

From the form of Eq. (18) it is possible to conclude that, since for realistic values of γ , $\gamma-4/3$ is a small number, dV/dt will initially be a constant. Also, since it is the square of dV/dt that approaches zero at some point, the solution will show a maximum volume followed by a collapse. Note that the maximum volume is not determined by a simple relation of pressure to p_∞ but is dependent on initial conditions.

Equation 18 seems to show a rather strong dependence on initial conditions and is not determined solely by the total laser energy absorbed. It is tempting to speculate that the pressure, as well as its spatial and temporal variation, and therefore the effectiveness of the laser lithotripsy may be strongly dependent on detailed characteristics of the laser pulse. Certainly it would seem that integration of Eq. (16) for a variety of energy absorption curves would be useful.

Discussion

The above analysis has not discussed the mechanisms of laser light absorption. Clearly, a more sophisticated consideration of vapor properties similar to that used in other laser materials interaction studies is required. The major difference in consideration of vapor properties is that in this case we are suggesting that the vapor expands slowly under quasi-hydrostatic conditions rather than the sonic expansion velocities which are reached when the laser material interaction occurs without a surrounding high density material.

The use of the acoustic approximation for the flow in the surrounding medium may be helpful in defining the usefulness of pressure monitors placed at some distance from the sight of the laser focus for measuring the strength of the laser-induced pressure pulse. This could, of course, be limited by non-uniform acoustic propagation and reflections.

We do, however, hope that the basic approximation of separating the flow into a quasi-static vapor bubble and an acoustic flow field will prove useful as each of the separate regions is considered in more detail.